RESEARCH ARTICLE

Extended flexible trailing-edge on the flow structures of an airfoil at high angle of attack

Xi He[1] · Qinfeng Guo[1] · Jinjun Wang[1]

Abstract

A two-dimensional time-resolved particle image velocimetry experiment was carried out to investigate the effect of flexible trailing-edge on the flow structures of an airfoil at high angle of attack. The experimental model was composed of a rigid NACA0020 airfoil and a flexible extended trailing-edge plate. The Reynolds number ranged from 1.42×10^4 to 3.57×10^4 (based on the model length). The kinematic characteristics of the flexible trailing-edge plate were first analyzed. While interacting with the fluid, the flexible plate performed a strongly periodic vibration. The plate presented more complicated deformation and larger amplitude with the increase of Reynolds number. The flow field was also captured in this study. It was found that the vibration of the flexible plate caused the generation and shedding of the trailing-edge vortex. Furthermore, the disturbance of plate vibration could propagate upstream and influence the formation of the leading-edge vortex in the separated shear layer. In the wake region, the alternative shedding processes of the leading- and trailing-edge vortices were coupled with the vibration of the plate. Besides, this study further scaled the vibration frequencies with a Strouhal number based on the wake width. The scaled Strouhal numbers were in the range of 0.14–0.21 for all Reynolds number cases tested, which indicated that the fluid–structure coupling led the flow to form a bluff-body wake.
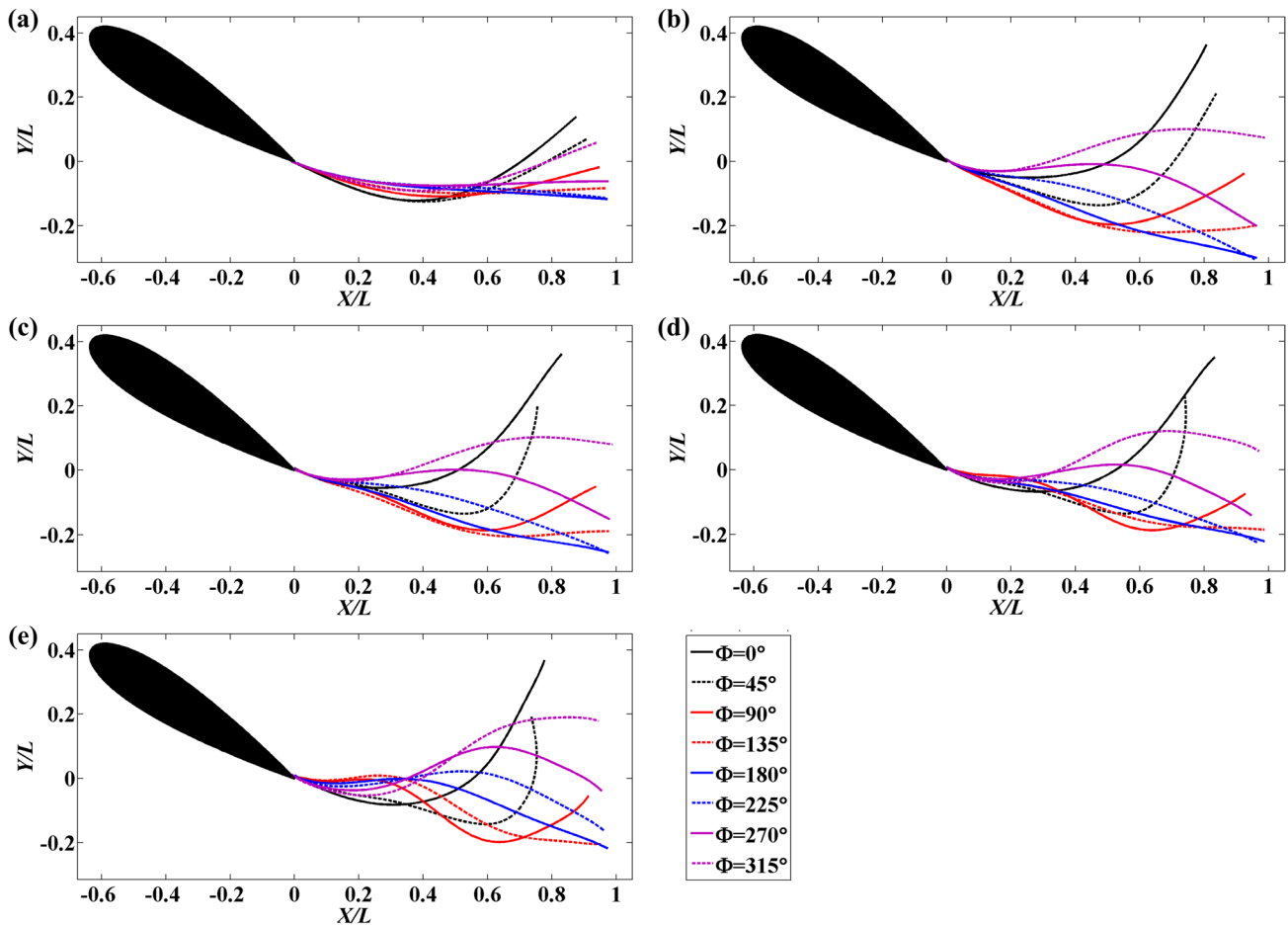
✉ Jinjun Wang
  jjwang@buaa.edu.cn

[1] Key Laboratory of Fluid Mechanics (Ministry of Education),
    Beijing University of Aeronautics and Astronautics,
    Beijing 100191, China

Graphic abstract

The vibration patterns of the flexible trailing-edge plate at various Reynolds numbers.

1 Introduction

Swimming performance of fish-like aquatic animals has always been a hot issue in the field of fluid mechanics. In the early studies of Lighthill (1970), Wu (1971), Katz and Weihs (1978), the flexible bodies of aquatic animals were found to have excellent hydrodynamic characteristics. The undulatory propulsion mode of such aquatic animals tends to improve their speed and hydrodynamic efficiency. A series of subsequent works were focused on the propulsion mechanism (Blake 1983; Triantafyllou et al. 1991; Wolfgang et al. 1999; Triantafyllou et al. 2000) and the movement of biomimetic fish models (Anderson et al. 1998; Triantafyllou et al. 2004; Heathcote and Gursul 2007; Dewey et al. 2013; Mackowski and Williamson 2015; David et al. 2017). Based on the rigidity of fish bodies, the structures of fish could be divided into four categories: anguilliform, subcarangiform, carangiform,

and thunniform (Lindsey 1978). Thunniform was further indicated to be the most efficient one in the review of Sfakiotakis et al. (1999). Accordingly, the movement of most fish can be simplified as the fluid–structure interaction of a rigid forebody and a flexible trailing-edge in an incoming flow. The flexible trailing-edge seems to be greatly important to the movement of entire body.

Numerous studies aimed to find out the mechanism of fluid–structure interaction of flexible plates or flags have been conducted. It was indicated in the soap film tunnel experiment by Zhang (2000) that the flexible flag performed three different modes with the flag length and flow velocity increasing: stretched straight mode, coherent flapping mode and chaotic flapping mode. The corresponding amplitude and frequency of each mode were also variable. Eloy et al. (2007, 2008) analyzed the flutter instability of cantilevered flexible plates theoretically and experimentally. They pointed out that the

instability of flexible plates or flags was due to the competition between destabilizing pressure forces and stabilizing bending stiffness. Further investigations of Connell and Yue (2007), Shelley and Zhang (2011) showed that the flutter modes of flag were related to the Reynolds number (Re), the mass ratio of flag-to-fluid and the flag rigidity. Chaotic flapping mode was easier to occur for the flag with higher Re, larger mass ratio and less rigidity. Shelly et al. (2005) investigated the interaction between heavy flags and fluid. It was emphasized that the body inertia played an important role in overcoming the stabilizing effects of finite rigidity and fluid drag. However, a majority of these works rarely considered the flow structures.

Besides, the fluid–structure interaction of flexible plates is a common phenomenon in nature and engineering. Watanabe (2002) indicated that the increase of paper printing speed would cause paper flutter and rupture, thereby reducing production efficiency. Allen and Smits (2001) placed a piezoelectric flexible plate in the wake of a bluff body, the Kármán vortex street of which could induce deformation and vibration of the plate, thus generating electricity. Giacomell and Porfiri (2011) proposed underwater energy harvesting from the flutter instability of the heavy flags. Moreover, such fluid–structure interaction phenomenon also has an effective application in stall control. Pantula (2008) suggested controlling post-stall separation of NACA0012 airfoil by attaching flexible fin on the upper surface of the airfoil. Using unsteady Reynolds-Averaged Navier–Stokes (RANS) solver combined with the immersed boundary method (IBM), it was found that the fluid–structure interaction between the fin and flow altered the flow structures to suppress separation, enhance lift and reduce the drag. Liu et al. (2009, 2010) supplemented the work of Pantula (2008) experimentally and indicated that drag reduction and oscillation suppression particularly for the natural low-frequency oscillation in deep stall were achieved using a flexible fin attached at a suitable location on the NACA0012 airfoil. Liu et al. (2007) discovered that attaching a static extended trailing-edge behind the NACA0012 airfoil could achieve lift enhancement at a small drag penalty. They prospected the great potential of flexible extended trailing-edge to improve the cruise flight efficiency and control separation.

Inspired by Liu et al. (2007, 2009) and other studies above, the present work conducted a particle image velocimetry (PIV) measurement to study a model consisting of a rigid NACA0020 airfoil and a flexible extended trailing-edge plate at high angle of attack. The main objectives are as follows: (1) study the kinematic characteristics of the flexible plate with the variation of Reynolds numbers (Sect. 3.1); (2) analyze the flow field to recognize the leading- and trailing-edge vortices and understand the corresponding evolution processes (Sects. 3.2–3.5); (3) investigate the fluid–structure coupling in the wake region as well as the shedding mode of the leading- and trailing-edge vortices (Sect. 3.6). The full paper is divided into the following parts: introduction, experimental method, results, discussion, and conclusion.

2 Experimental method

The present experiment was carried out in the low-speed recirculation water tunnel at Beijing University of Aeronautics and Astronautics. The test section of the water tunnel is 3 m-long with a cross-section size of 0.6 m-wide × 0.7 m-deep. The side and bottom walls are made of transparent plexiglass. The maximum freestream velocity (U_∞) is up to 0.40 m/s with the turbulent intensity (σ) less than 1% in this water tunnel. In the present experiment, U_∞ was in the range of 0.12–0.30 m/s and the fluid temperature was around 18.5 °C.

2.1 Model design

As shown in Fig. 1, the experimental model is composed of an aluminum NACA0020 airfoil and a flexible extended trailing-edge plate. The coordinate origin is selected at the end of the airfoil. X and Y represent streamwise and vertical directions, respectively. With the chord length of the airfoil (C) to be 60 mm and the size of the flexible plate to be 80 mm (length L) × 80 mm (span W) × 0.1 mm (thickness t), the corresponding characteristic length ($D = C + L$) was 140 mm, resulting in the Reynolds number based on D (Re_D) in the interval of $1.42 \times 10^4 \sim 3.57 \times 10^4$. The material of this flexible plate was transparent polycarbonate with the Young's modulus, Poisson ratio and density of $E = 780$ MPa, $\mu = 0.4$ and $\rho_m = 1.2$ g/cm^3, respectively. The reduced velocity used by Eloy et al. (2008) is

$$U_\infty^* = U_\infty \sqrt{\frac{\rho_f W L^3}{B}}, \tag{1}$$

where ρ_f is the water density, $B = Et^3W/12\left(1 - \mu^2\right)$ is the rigidity of the plate. The reduced velocity is the nondimensional parameter for the ratio between fluid inertia force and elastic bending force. In this paper, the reduced velocity was in the range of 10.0–25.0 for the measured freestream velocities. Considering only one kind of flexible plate was tested in this work, Re_D and U_∞^* were in direct proportion to freestream velocity. Hence, Re_D was used as the nondimensional parameter to analyze flow characteristics. Referring to the study of Shelly et al. (2005), three carbon-fiber strips 3 mm-wide were attached on the flexible plate along spanwise direction and the distance between adjacent strips (S) was 30 mm. Accordingly, the chordwise rigidity of the flexible plate was much lower than the spanwise rigidity. Thus, the two-dimensional motion property of the flexible plate was greatly improved.

Fig. 1 Experimental model
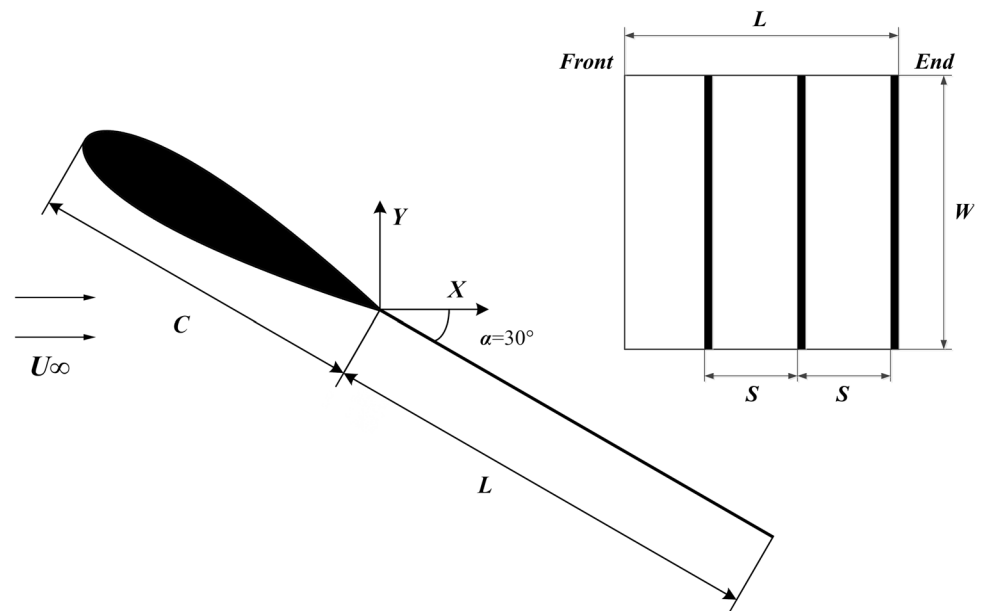
To facilitate connection, a slot was cut along the chord in the rear of the airfoil into which the flexible plate could be inserted. As a result, the trailing-edge plate could be approximated to a cantilever plate with one end fixed and the other end free. For comparison, a rigid aluminum trailing-edge plate with the same size was also adopted to be a reference.

The model was vertically installed in the water tunnel with the plate midspan positioned at depth halfway of the tunnel as shown in Fig. 2. The angle between the airfoil chord and freestream (α) was 30°, which belonged to the post-stall angle of attack. A plexiglass plate 1 m-long and 10 mm-thick was equipped on the top tunnel surface to minimize surface waves.

2.2 Particle image velocimetry

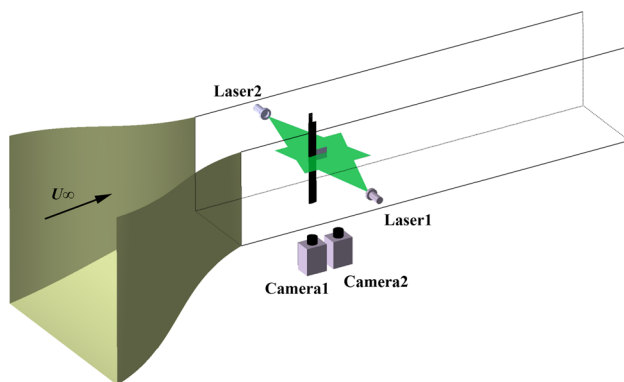The schematic diagram of the PIV experimental setup is illustrated in Fig. 2. The high-speed laser Beamtech Vlite

Fig. 2 Schematic diagram of the PIV experiment

Hi-527 with the frequency up to 1 kHz was used in the present two-dimensional time-resolved PIV (2D-TRPIV) experiment as a light source. The plane at the plate midspan was adopted as the measuring plane. To get the required flow field, two parallel laser sheets of approximately 1 mm-thick were irradiated from both sides of the model to illuminate the measured area. Hollow glass beads with diameter of 10 μm were employed as tracer particles and the density was 1.05 g/mm^3, which is close to the water density. Two synchronous high-speed Fastcam Photron SA2 CMOS cameras mounted along streamwise direction were employed in the present study to capture the motion of flexible trailing-edge plate and flow structures simultaneously. The sampling speed was in the range of 200–400 Hz due to the freestream velocity. The resolution of each camera was 2048×2048 pixels and the field of view (FOV) was about 170 mm×170 mm, resulting in the magnification being 0.083 mm/pixel. The raw images were processed based on the multiple iterative Lucas–Kanade algorithm (MILK) (Champagnat et al. 2011; Pan et al. 2015) to obtain original velocity field. The interrogation window size was set to be 32×32 pixels with 75% overlap and the number of velocity vectors were 256×256.

2.3 Deformation

The raw images not only recorded the distributions of tracer particles, but also contained the information of the flexible plate positions. With the aim to obtain these positions, a boundary recognition algorithm was proposed in this study. The first step was to select the region of the flexible plate. This region must completely contain

the flexible plate and should be as small as possible to reduce the cost of computation. Afterwards, using a binary method, the region with a grey value larger than the threshold was marked as value "1" and conversely, the value was "0". The principle of this binary method was to keep the flexible plate as continuous as possible. A result of this step is shown in Fig. 3a. Then, another threshold was set using the MATLAB function "bwareaopen" to eliminate the tracer particles with the area less than this threshold in Fig. 3a and the position matrix of the pure flexible plate was retained, as shown in Fig. 3b. Finally, a single-valued function in X or Y direction was obtained by getting the median of this position matrix. Consequently, the curve of flexible plate was acquired by interpolation and polynomial fitting methods.

2.4 Post-processing methods

To facilitate a deep comprehension of the flow field, some post-processing methods were adopted. This section provides brief introductions to these methods.

2.4.1 Phase-averaging

The phase-averaging method is a good way to study quasi-periodic flow. The common approach is to select a quasi-periodic reference signal in the flow to determine different phases. In the previous studies, Kim et al. (2006) adopted the streamwise velocity at a certain point in the flow field as a reference signal. Cantwell and Coles (1983) used the pressure signal near the cylinder separation point as a reference signal. Zhou et al. (2002, 2006) referred the vertical

Fig. 3 Recognition of the flexible plate

velocity in the wake region for phase-averaging. It could be seen that all of these works used flow field signals such as velocity and pressure. However, in this fluid–structure interaction study, it was the vibration of the plate that significantly and directly influenced the flow field. Therefore, it was more suitable to adopt the position signal of the plate endpoint as a reference signal rather than the velocity signals.

2.4.2 Vortex identification

For vortex identification, it was indicated that the velocity gradient tensor of the flow field and its eigenvalues contained a lot of information about the flow structures (Zhou et al. 1999; Adrian et al. 2000). For two-dimensional flow, the velocity gradient tensor matrix is

$$\nabla u = \begin{pmatrix} \frac{\partial u}{\partial x} & \frac{\partial u}{\partial y} \\ \frac{\partial v}{\partial x} & \frac{\partial v}{\partial y} \end{pmatrix}. \tag{2}$$

Assuming there is a pair of complex eigenvalues, that is $\lambda_{cr} \pm i \cdot \lambda_{ci}$, where λ_{cr} and λ_{ci} represent the real and imaginary parts of the complex eigenvalues, respectively. λ_{ci}, which is called the swirl strength, can reflect the strength of local vortex structures. When $\lambda_{ci} > 0$, it is considered there exists a vortex. When $\lambda_{ci} \leq 0$, there is no vortex structure. The identification of vortices by this method is independent on coordinate systems due to the adoption of velocity gradient tensor. Furthermore, the swirl strength method can distinguish the real vortex structures from the shear layer with large vorticity.

2.4.3 Fourier mode decomposition

Compared with the single-point fast Fourier transformation (FFT), the Fourier mode decomposition (FMD) method proposed by Ma et al. (2015) can provide frequency information of the global flow field. Besides, FMD can effectively extract the dynamic mode along with its amplitude and phase according to the selected characteristic frequency based on the global power spectrum. For the flow region of interest, single-point discrete Fourier transformation (DFT) is conducted to velocity data at every mesh node to get a Fourier mode matrix c_k.

$$c_k = \frac{1}{N} \sum_{n=0}^{N-1} F_n e^{-i\left(\frac{2\pi k}{N}\right)n}, \tag{3}$$

where N is total sampling number, F_n is the original velocity matrix. Furthermore, the global power spectrum density (PSD_k) can be defined as
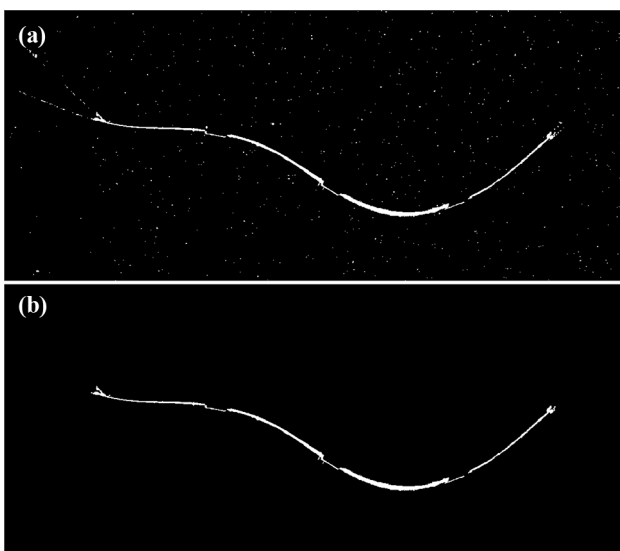
$$PSD_k = \left\| \frac{2N|c_k|^2}{\pi f_s} \right\|, \tag{4}$$

where $\|\bullet\|$ is the Frobenius norm, f_s is the sampling frequency. The frequency characteristics of the dynamic structures can be determined by detecting the peaks in the power spectrum. The FMD method can decompose the global flow into individual characteristic frequencies, while the global mode extracted by the proper orthogonal decomposition (POD) method (Miyanawala and Jaiman 2019; Deng et al. 2017) may be related to multiple characteristic frequencies.

2.4.4 Cross-correlation

Cross-correlation is an important method in fluid–structure interaction research (Timpe et al. 2013; Bleischwitz et al. 2017). Commonly, the fluctuating signals at two selected points are adopted for spatial–temporal cross-correlation, which can be expressed as

$$R_{S_1 S_2}(x_0, y_0, x_1, y_1, t, \tau) = \frac{\overline{S_1(x_0, y_0, t) S_2(x_1, y_1, t + \tau)}}{\sigma_{S_1} \sigma_{S_2}}, \tag{5}$$

where R is the correlation coefficient between the two signals: S_1 and S_2. (x_0, y_0) and (x_1, y_1) are the spatial locations of the two selected points. τ is the time lag. $\overline{\bullet}$ represents the averaging process. σ_{S_1} and σ_{S_2} are the auto-covariance matrix of the two signals. When $\tau = 0$, the formula is reduced to spatial cross-correlation with zero time lag. Accordingly, the correlation coefficient can indicate either in-phase or out-of-phase relationships between the two signals. When $\tau \neq 0$, phase lead-lag properties of the two signals can be derived from cross-correlation.

3 Results

3.1 Kinematic characteristics

In this study, the flexible trailing-edge plate attached to the airfoil would vibrate while interacting with the surrounding fluid. The vibration frequencies of the plate (f_{pl}) were attained by conducting FFT on the vertical movement at the end of the plate. The spectra of plate vibration at $Re_D = 1.42 \times 10^4$ and 3.57×10^4 are shown in Fig. 4 and the power spectrum density (PSD) is normalized by its maximum value in each case. It is obvious that the vibration of this flexible plate is a strongly periodic motion. The vibration frequencies of all Re_D cases are listed in Table 1, in which the frequency increases from 0.62 to 1.54 Hz.

According to Fig. 4 and Table 1, the vibration of the flexible plate is indeed a periodic motion. As a result, a relatively accurate phase-averaging process based on the position signal of the plate endpoint could be conducted. To intuitively embody the motion of the flexible plate, the phase-averaged vibration patterns in one cycle are presented in Fig. 5. Due to the position of coordinate origin, L was selected as the characteristic length to display the positions of the flow field relative to the plate. In each Re_D case, the phase $\Phi = 0°$ is defined corresponding to the phase when the end of the plate vibrates to the highest vertical position. It can be found

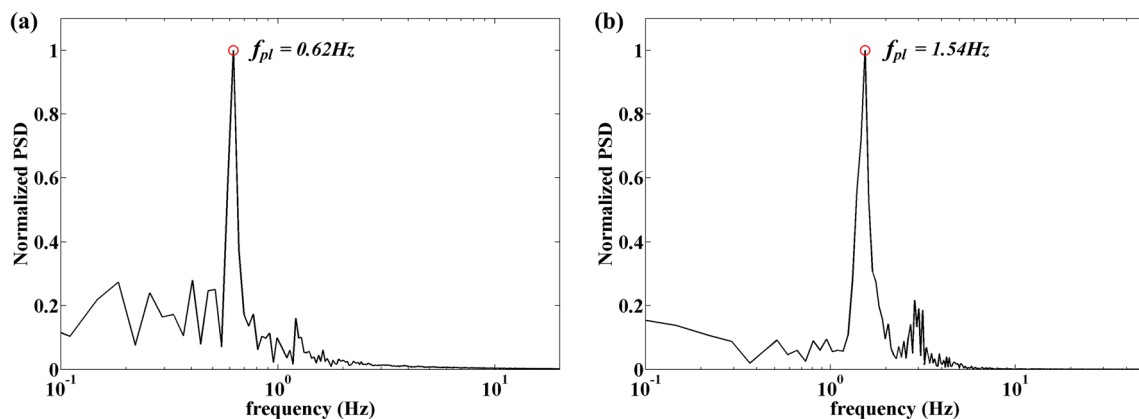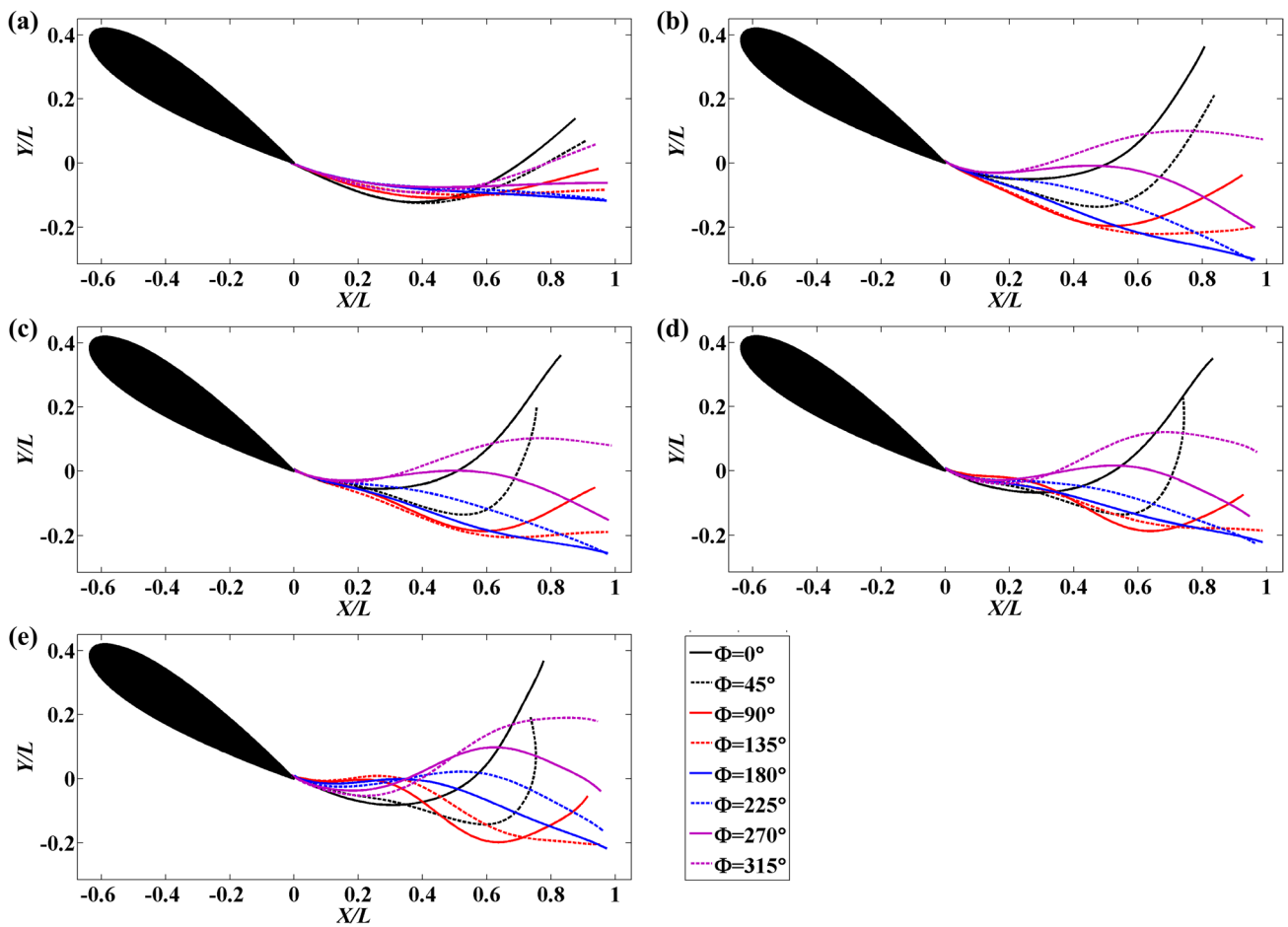**Fig. 4** Frequency spectra of the flexible trailing-edge plate. **a** $Re_D = 1.42 \times 10^4$; **b** $Re_D = 3.57 \times 10^4$

Table 1 Plate vibration frequencies at different Re_D

Re_D	1.42×10^4	1.78×10^4	2.14×10^4	2.5×10^4	2.84×10^4	3.2×10^4	3.57×10^4
f_{pl} (Hz)	0.62	0.73	0.78	0.88	0.99	1.25	1.54

Fig. 5 Phase-averaged vibration patterns in one cycle. **a** $Re_D = 1.42 \times 10^4$; **b** $Re_D = 2.5 \times 10^4$; **c** $Re_D = 2.84 \times 10^4$; **d** $Re_D = 3.2 \times 10^4$; **e** $Re_D = 3.57 \times 10^4$

that the end of the plate reaches the lowest vertical position at around $\Phi = 180°$ for all Re_D cases. Moreover, the vibration pattern of the plate seems to present more complicated deformation and larger amplitude with the increase of Re_D.

As illustrated in Fig. 6, the vibration parameters of the flexible plate change with Re_D. In Fig. 6a, the vibration frequency of the plate increases monotonously with increasing Re_D. Figure 6b indicates the relationship between Re_D and the vibration amplitude (A), which is equal to the average vertical excursion of the plate end. The characteristic length D is used as the nondimensional length scale for vibration amplitudes. It is found that the vibration amplitude sharply increases from $Re_D = 1.42 \times 10^4$ to $Re_D = 2.5 \times 10^4$. After that, the increase rate slows down. The vibration frequency and amplitude can be reflected by a comprehensive parameter of Strouhal number based on the vibration amplitude (St_A). It is defined as $St_A = f_{pl} A / U_\infty$. As shown in Fig. 6c, St_A seems to increase linearly with Re_D. The fitting equation is

$$St_A = 6.23 \times 10^{-6} Re_D, \tag{6}$$

where the correlation coefficient is 0.97, indicating a highly linear correlation between St_A and Re_D.

3.2 Evolution of trailing-edge vortex

The phase-averaged streamlines are presented in Fig. 7 with the phase interval of 45°, where the corresponding Re_D are equal to 1.42×10^4 and 3.57×10^4, respectively. The streamwise and vertical positions are normalized by L. In the first column of Fig. 7 ($Re_D = 1.42 \times 10^4$), there always exists a separation region at the leeward airfoil surface. At $\Phi = 0°$ (Fig. 7a) the end of the flexible plate is at the highest vertical position, there is a counter-clockwise vortex (hereinafter referred to as the trailing-edge vortex) near the end of plate. Subsequently, the flexible plate moves towards the negative Y direction, resulting in the extrusion of the trailing-edge vortex. When Φ reaches 90° (Fig. 7e), the trailing-edge vortex goes above the flexible plate. As Φ continues to increase, the trailing-edge vortex gradually sheds from the plate and then dissipates downstream. The trailing-edge

(a)

(b)

(c)
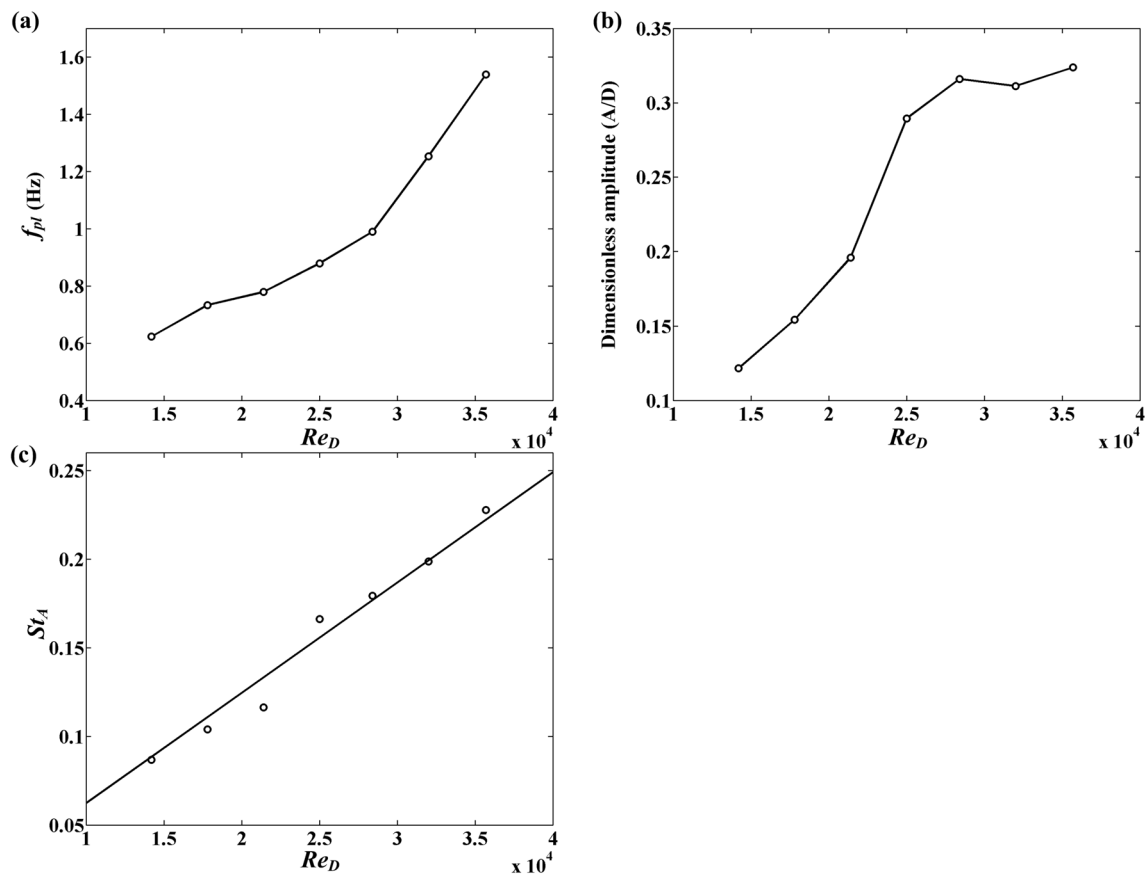
Fig. 6 Variations of kinematic parameters with Re_D. **a** Vibration frequency vs. Re_D; **b** vibration amplitude vs. Re_D; **c** Strouhal number vs. Re_D

vortex is no longer seen from the streamlines at $\Phi = 180°$ (Fig. 7i) as the end of the plate reaches the lowest vertical position. Simultaneously, the streamlines of the separation region are closed near the end of the flexible plate. Then the flexible plate begins to move towards the positive Y direction and the trailing-edge vortex appears beneath the plate at $\Phi = 315°$ (Fig. 7o).

In general, the evolution of the trailing-edge vortex can be summarized as the process that the trailing-edge vortex generates and accumulates beneath the flexible plate and then it is extruded by the plate. After that, the trailing-edge vortex sheds from the plate and dissipates downstream. In one cycle, only one trailing-edge vortex is generated at the end of the flexible plate. In the second column of Fig. 7 ($Re_D = 3.57 \times 10^4$), the evolutionary process of the trailing-edge vortex still exists.

For comparison, the time-averaged flow field of the rigid trailing-edge plate case is shown in Fig. 8. Compared with the flexible case, the rigid case has a much larger separation region with no wake formation in the FOV. It means that the existence of the flexible trailing-edge plate can greatly suppress the post-stall separation at high angle of attack in contrast to the airfoil with rigid plate. Comparing the

streamlines of rigid plate case at different Re_D, no obvious difference is found.

3.3 Evolution of leading-edge vortex

Based on the phase-averaged flow field, the vortex structures were identified through swirl strength (λ_{ci}) method. The phase-averaged vortex structures are shown in Fig. 9 with the phase interval of 45°. The red and blue structures represent the counter-clockwise and clockwise vortices, respectively. In this investigation, vortices are named by the combination of a number and an abbreviation, where the number represents the order of the cycle: the current cycle is defined as "1" and the previous cycle is "− 1". The abbreviation indicates the source of vortex: LEV is the leading-edge vortex and TEV is the trailing-edge vortex. Similar to Fig. 7, the generation, shedding, and dissipation processes of the trailing-edge vortex (1TEV) can also be seen in Fig. 9.

Besides, compared with Fig. 7, more detailed information about the evolution of the shear layer at the leeward side of the model is given in Fig. 9. In the first column of Fig. 9 ($Re_D = 1.42 \times 10^4$), when $\Phi = 0°–90°$, the shear layer
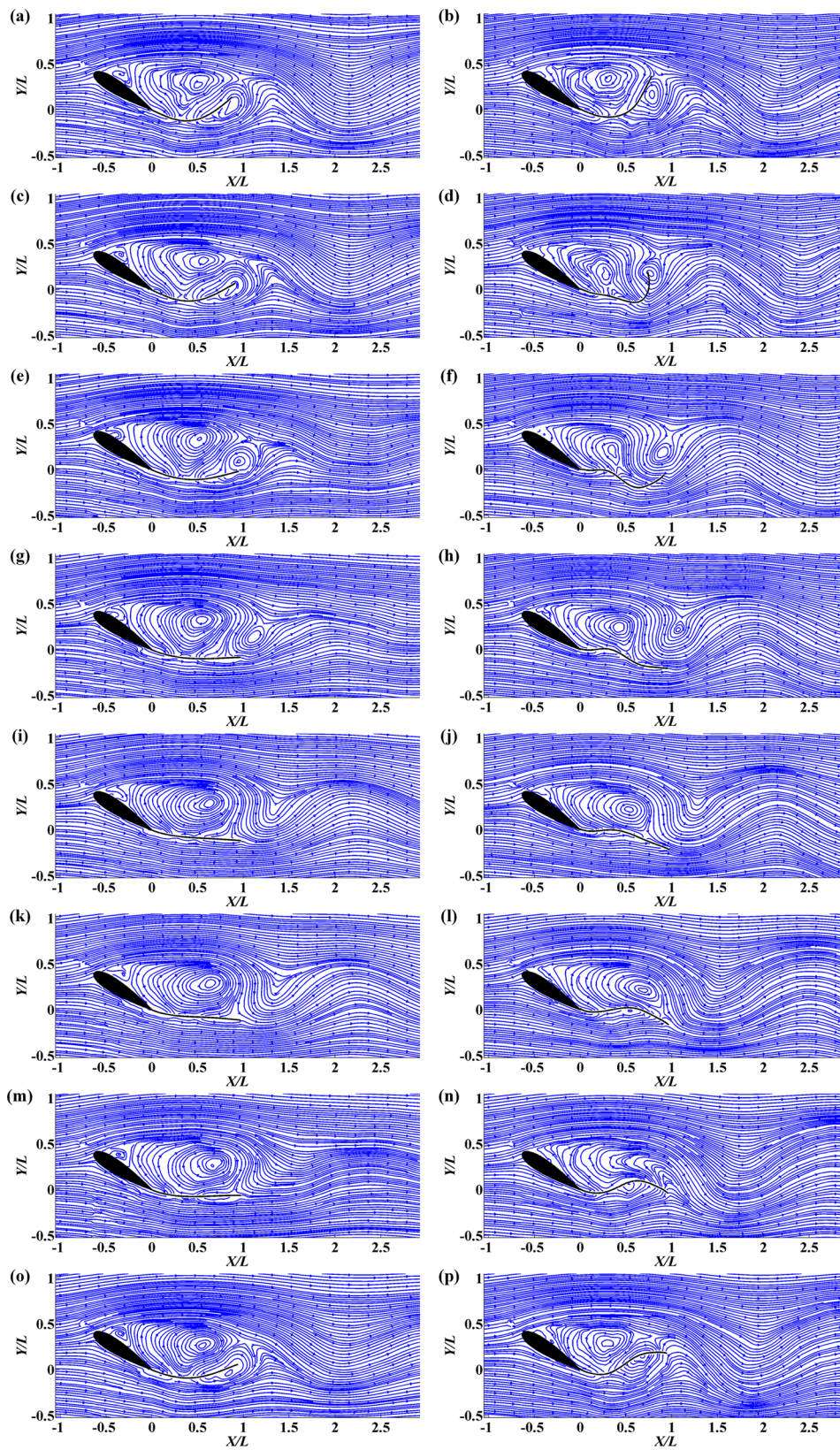
Fig. 7 Phase-averaged streamlines of flexible trailing-edge plate cases. **a, c, e–o** $Re_D = 1.42 \times 10^4$; **b, d, f–p** $Re_D = 3.57 \times 10^4$; **a, b** $\Phi = 0°$; **c, d** $\Phi = 45°$; **e, f** $\Phi = 90°$; **g, h** $\Phi = 135°$; **i, j** $\Phi = 180°$; **k, l** $\Phi = 225°$; **m, n** $\Phi = 270°$; **o, p** $\Phi = 315°$
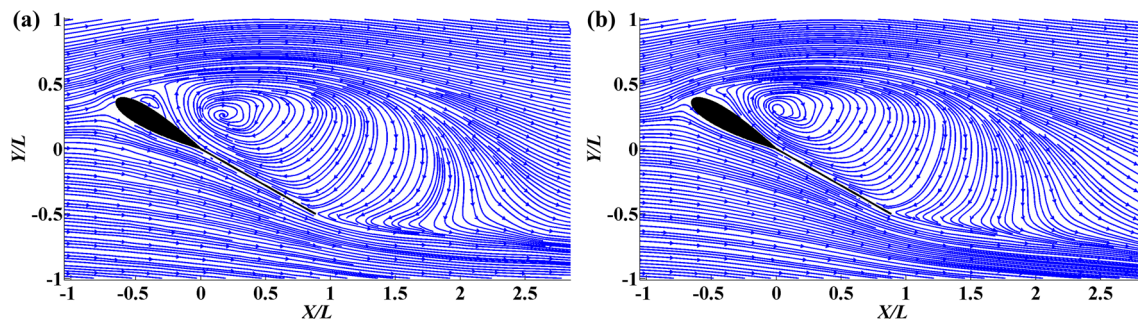
Fig. 8 Time-averaged streamlines of rigid trailing-edge plate cases. **a** $Re_D = 1.42 \times 10^4$; **b** $Re_D = 3.57 \times 10^4$

performs a series of small-scale vortices along streamwise direction before $X/L = 1$. The large-scale clockwise vortex after $X/L = 1$ is the leading-edge vortex formed in the previous cycle (-1LEV). When $\Phi = 90°$–$225°$, the small-scale vortices gradually merge into a large-scale leading-edge vortex (1LEV) near $X/L = 0.8$, especially in Fig. 9i, k. It can also be seen that the leading-edge vortex (-1LEV) has completely dissipated downstream when the current leading-edge vortex (1LEV) generates. Intuitively from the vortex structures in Fig. 9, the existence of the trailing-edge vortex hinders the development of the shear layer, resulting in the small-scale vortices merging into a large-scale leading-edge vortex. It should be noticed that the generation and shedding processes of the leading- and trailing-edge vortices occur only once in one flow cycle. These results are also supported by the second column of Fig. 9 ($Re_D = 3.57 \times 10^4$). However, the dissipation of the leading- and trailing-edge vortices is faster at $Re_D = 3.57 \times 10^4$.

A detailed cross-correlation analysis was further conducted to study the relationship of the leading- and trailing-edge vortices at their initial shedding positions. The initial shedding positions are distinguished from the wake region. In accordance with Fig. 9, the initial shedding positions of these two structures at $Re_D = 1.42 \times 10^4$ are marked by point A and point B in the time-averaged vorticity contour shown by Fig. 10. The vertical displacement at the end of the flexible plate (marked with the green pentagram) was selected as the correlation signal due to its largest fluctuations. Therefore, Eq. (5) can be rewritten as

$$R_{y'\omega}\left(x_0, y_0, x_1, y_1, t, \tau\right) = \frac{\overline{y'\left(x_0, y_0, t\right)\omega\left(x_1, y_1, t + \tau\right)}}{\sigma_{y'}\sigma_{\omega}}, \quad (7)$$

where y' is the vertical plate displacement fluctuations at the plate end, ω is the instantaneous vorticity at point A or B.

Figure 11a shows time histories of y', ω_A, and ω_B, which are normalized by their maximum absolute values. Due to the direction of the vortices, the valley values of ω_A and

peak values of ω_B, respectively, represent the maximum vorticities of the leading- and trailing-edge vortices. It can be seen that ω_B slightly lags behind y', which indicates the plate vibration is closely followed by the shedding of the trailing-edge vortex. Moreover, y' and ω_A reach their valley values almost simultaneously. It means the leading-edge vortex attains the maximum vorticity when the plate endpoint reaches the lowest vertical position. Phase lead–lag properties of these three periodic signals can be derived from Eq. (7) and are presented in Fig. 11b. $\Delta\Phi$ is the phase lag, which is defined as $\Delta\Phi = 360\tau \cdot f_{\text{pl}}(°)$, where τ is the time lag. As shown, $R_{y'\omega_B}$ reaches its maximum peak value at $\Delta\Phi$ around $60°$, while $R_{y'\omega_A}$ reaches its minimum valley value at $\Delta\Phi$ around $200°$. There is a phase lag of around $140°$ between the leading- and trailing-edge vortices at their initial shedding positions. It can be inferred from this phase lag that the trailing-edge vortex actually hinders the development of the shear layer, resulting in the formation and initial shedding of the leading-edge vortex.

In brief, the shedding process of the trailing-edge vortex has an important influence on the formation and initial shedding of the leading-edge vortex. From the vortex structures and correlation analysis, the trailing-edge vortex hinders the development of the shear layer, causing the small-scale vortices' merging into a large-scale leading-edge vortex. The generation process of the leading-edge vortex is further elaborated in Sect. 3.4, which shows the existence of vortex merging in the shear layer.

3.4 Mechanism of leading-edge vortex generation

For the generation of the leading-edge vortex, it was only observed in Fig. 9 that the small-scale vortices in the shear layer merged into a large-scale vortex. However, more accurate results were not given. Therefore, frequency characteristics of the shear layer were analyzed.

Figure 12 presents the vertical velocity spectra of the shear layer at different streamwise positions at $Re_D = 1.42 \times 10^4$. Before $X/L = 0.7$, the frequency spectra show higher frequency peak values. While at $X/L = 0.7$,

Fig. 9 Phase-averaged vortex structures of flexible trailing-edge plate cases. **a, c, e–o** $Re_D = 1.42 \times 10^4$; **b, d, f–p** $Re_D = 3.57 \times 10^4$; **a, b** $\Phi = 0°$; **c, d** $\Phi = 45°$; **e, f** $\Phi = 90°$; **g, h** $\Phi = 135°$; **i, j** $\Phi = 180°$; **k, l** $\Phi = 225°$; **m, n** $\Phi = 270°$; **o, p** $\Phi = 315°$
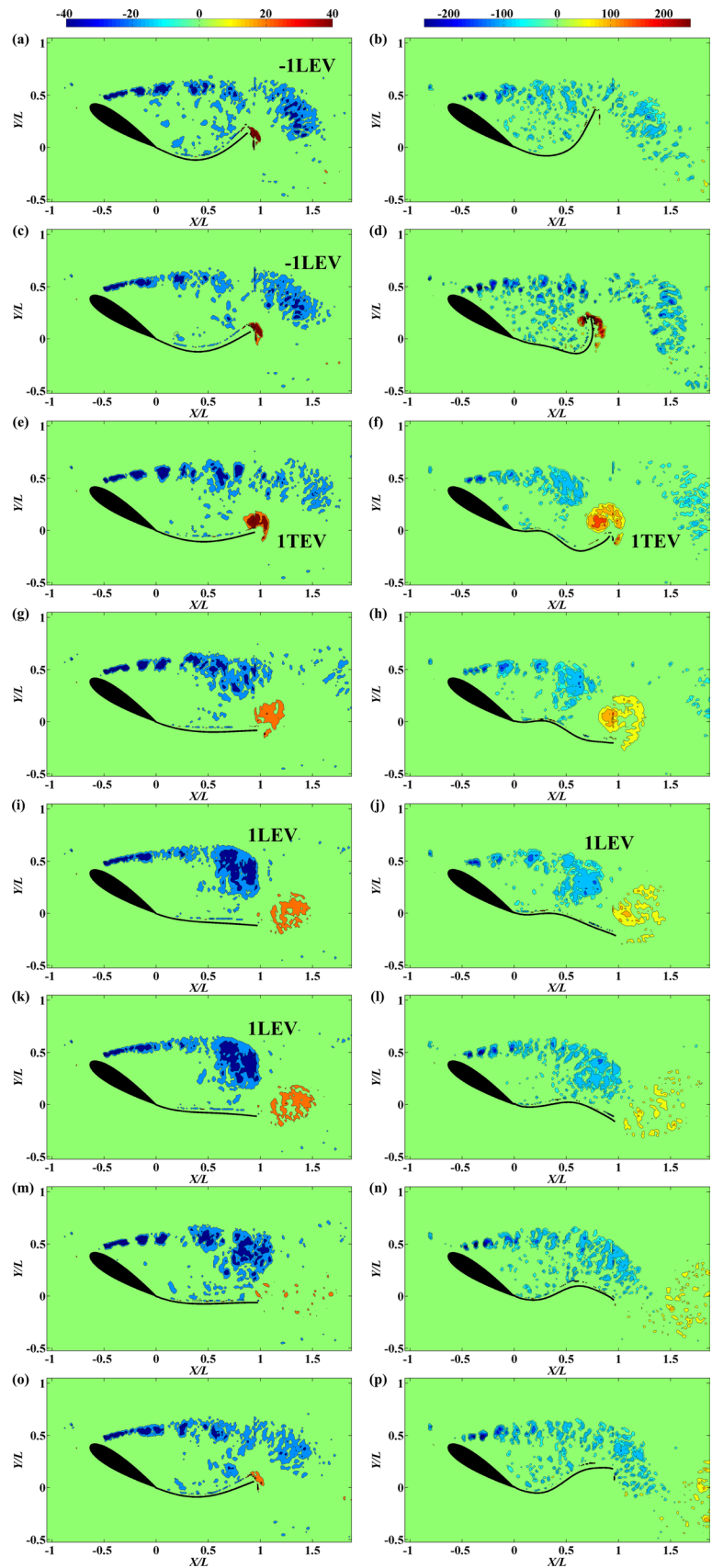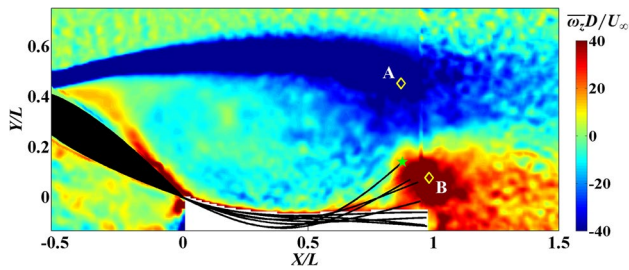
Fig. 10 Time-averaged vorticity contour of local flow field at $Re_D = 1.42 \times 10^4$. Point A and point B represent the initial shedding positions of the leading- and trailing-edge vortices. The plate end is indicated with the green pentagram

the peak of 0.62 Hz that is the same as the vibration frequency in Table 1 appears, indicating the disturbance of the plate vibration propagates to the position of $X/L = 0.7$. Similarly, the spectra of the shear layer at $Re_D = 2.5 \times 10^4$ and $Re_D = 3.57 \times 10^4$ were analyzed. It was found that the disturbance of the plate vibration propagated to $X/L = 0.2$ and $X/L = -0.1$, respectively. These results indicated that the influence of plate disturbance could propagate upstream towards the shear layer and was more advanced with the increase of Re_D.

Besides, Fourier mode decomposition (FMD) was conducted to analyze the local flow field around the shear layer, thus investigating the generation of the leading-edge vortex. Simultaneously, the dynamic modes at different frequencies were obtained.

The local root mean square contour of streamwise velocity fluctuation (u_{rms}) around the shear layer is shown in Fig. 13a at $Re_D = 1.42 \times 10^4$. The region with large fluctuation values is selected with the black box in the contour. By conducting FMD in this region, the power spectrum of the local flow field could be attained. As shown in Fig. 13b, there exists the peak with frequency of 0.62 Hz, which is in accordance with the vibration frequency of the plate. It means the disturbance of the flexible plate vibration has

propagated to the shear layer. There are other two peaks at higher frequencies of $f = 2.42$ Hz and $f = 5.13$ Hz. In this paper, the resolution of the dominant frequency is ± 0.03 Hz, which means the dominant frequency is 0.62 ± 0.03 Hz. Accordingly, the fourth and eighth harmonics of the dominant frequency are 2.48 ± 0.12 Hz and 4.96 ± 0.24 Hz, respectively. The frequencies of $f = 2.42$ Hz and $f = 5.13$ Hz, which are exactly in these two ranges, can be considered as the fourth and eighth harmonics of the dominant frequency.

The dynamic Fourier modes corresponding to the frequencies above could be obtained by FMD method. In reference to the work of Wang et al. (2018), the vertical velocity mode was selected for analysis. From Fig. 14a and b, it can be known that compared with the frequency of $f = 5.13$ Hz, the size of the mode and the distance between adjacent structures are larger at $f = 2.42$ Hz. And the corresponding positions are closer to downstream. As mentioned above, the frequencies of $f = 2.42$ Hz and $f = 5.13$ Hz can be considered as the fourth and eighth harmonics of the dominant frequency. So $f = 2.42$ is approximately the sub-harmonic component of $f = 5.13$. Considering the conclusion of Yarusevych et al. (2006, 2009), it was inferred that the vortex merging occurred during the development of the shear layer. The roll-up vortices (RV) in the shear layer merged to form the merged roll-up vortices (MRV). Figure 14c shows the Fourier mode at the plate vibration frequency ($f = 0.62$ Hz). In Sect. 3.6, this mode is further discovered to be a local part of Fig. 23, which indicates that the flow field begins to couple with the plate vibration in the downstream of the shear layer.

Furthermore, Fig. 15 shows the instantaneous local vorticity field at $Re_D = 1.42 \times 10^4$. The time sequences are t, $t + 0.135$ s, $t + 0.27$ s, and $t + 0.405$ s, respectively. From Table 1, the flow period at $Re_D = 1.42 \times 10^4$ is $1/0.62 \approx 1.6$ s. Therefore, the four snapshots represent the 1/4 cycle of the flow field. It can be seen that two roll-up vortices (1RV and 2RV) generate in the 1/4 cycle. Meanwhile, the two roll-up vortices formed in the previous cycles (-2RV and -1RV)
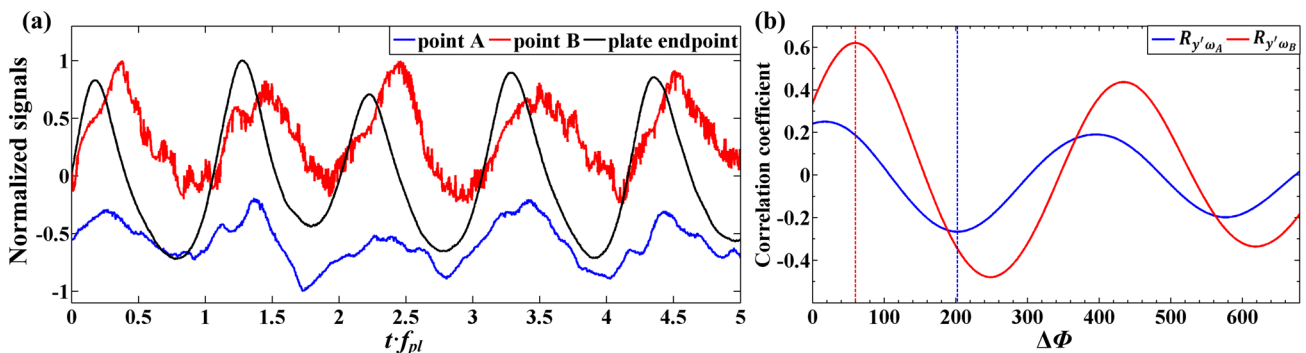
Fig. 11 Relationships of the leading- and trailing-edge vortices and the plate. **a** Time histories of the selected signals; **b** correlation coefficients with phase lag
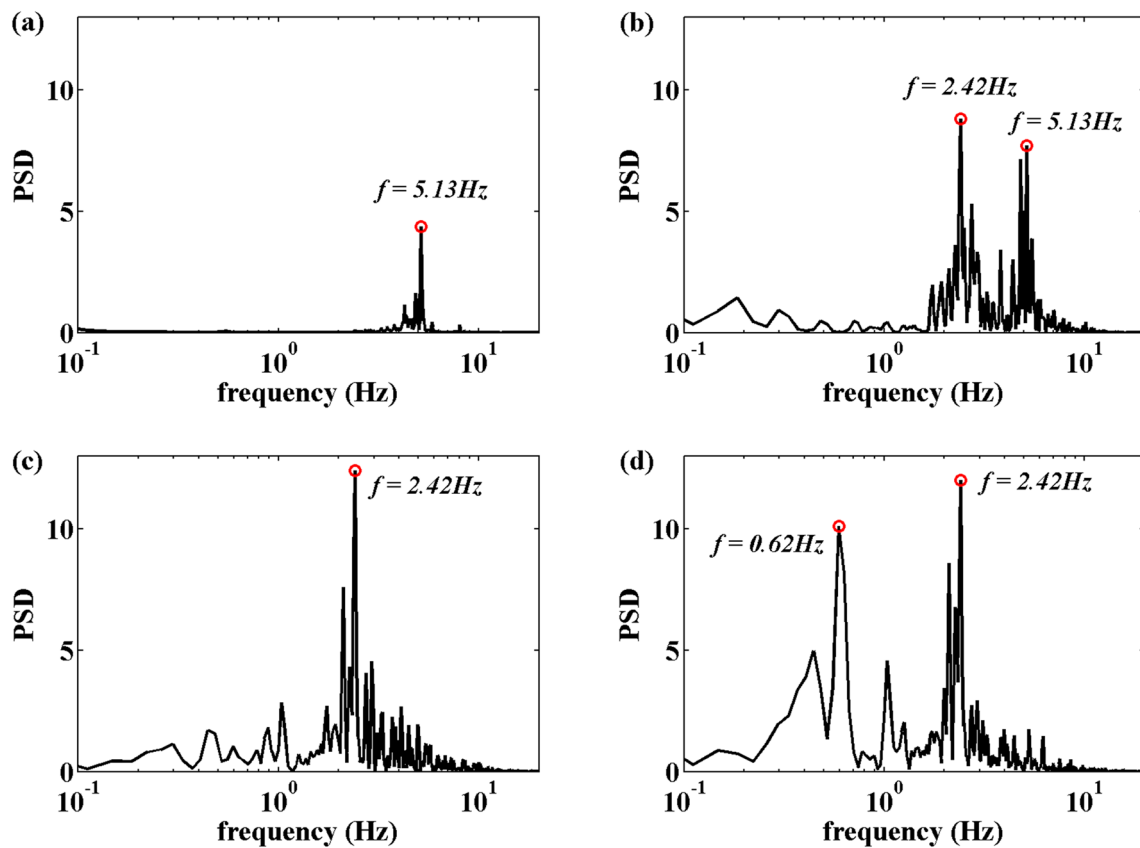
Fig. 12 Frequency spectra of vertical velocities in the airfoil shear layer at $Re_D = 1.42 \times 10^4$. **a** $X/L = -0.1$; **b** $X/L = 0.2$; **c** $X/L = 0.5$; **d** $X/L = 0.7$
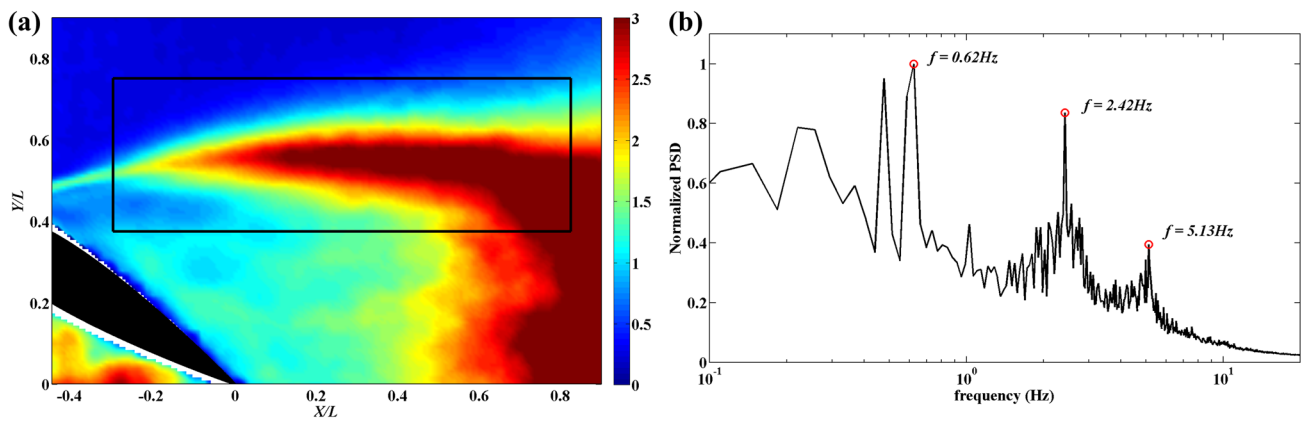

Fig. 13 Local FMD around the airfoil shear layer at $Re_D = 1.42 \times 10^4$. **a** Local root mean square contour of streamwise velocity fluctuation; **b** power spectrum of the local flow field

merge into a merged roll-up vortex (1MRV). It means that the period of MRV is about 0.4 s with the frequency about 2.5 Hz. The frequency of RV is twice as large as that of MRV. These results are in accordance with the frequencies of the Fourier modes described in Fig. 14a and b.

Similar process of vortex merging is also found at $Re_D = 2.84 \times 10^4$ in Fig. 16. The time sequences are t,

$t + 0.043$ s, $t + 0.087$ s, and $t + 0.13$ s, respectively. Compared with Fig. 15, vortex merging occurs at a more advanced streamwise position. Consequently, vortex merging is found in the separated shear layer in both low and high Re_D cases.

Overall, the leading-edge vortex generates from the coherent structures in the separated shear layer. Initially, the development of shear layer is similar to the process

(a)

(b)

(c)
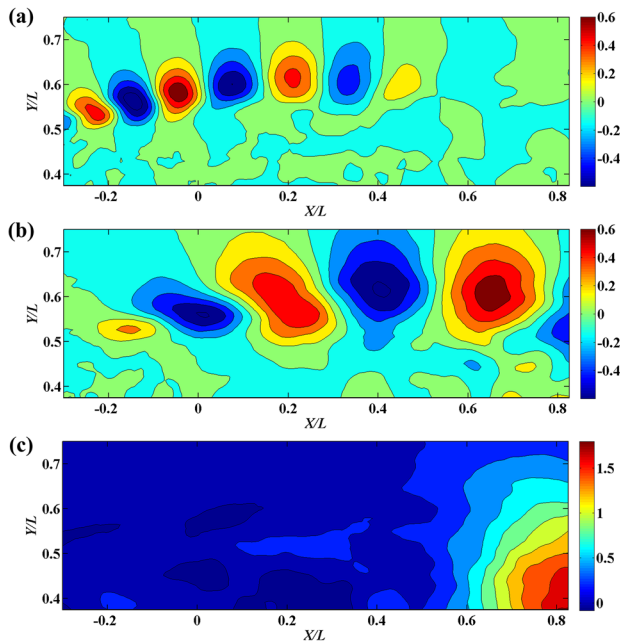
Fig. 14 Local Fourier modes based on vertical velocity at $Re_D = 1.42 \times 10^4$. **a** $f = 5.13$ Hz; **b** $f = 2.42$ Hz; **c** $f = 0.62$ Hz

described by Yarusevych et al. (2006, 2009). The existence of Kelvin–Helmholtz instability in the shear layer brings disturbances to the flow field. Then the disturbances amplify and eventually result in the formation of roll-up vortices. Following the roll-up process, the sub-harmonic component in the spectrum increases (as shown in Fig. 12). This leads to the merging of roll-up vortices to form the merged roll-up vortices. Subsequently, the shear layer is hindered by the trailing-edge vortex and gradually evolves into a leading-edge vortex.

3.5 Statistical characteristics

In the present study, the statistical characteristics of the flow field were analyzed. Figure 17 presents the minimum value evolution of the time-averaged streamwise velocity (U) along downstream direction at $Re_D = 3.57 \times 10^4$, and the time-averaged streamwise velocity distributions at the chosen four streamwise positions ($X/L = 0.4, 1.1, 1.8$ and 2.5) are further shown in Fig. 18. The black and blue lines represent the flexible and rigid plate cases, respectively. U is nondimensionalized by U_∞. As shown in Fig. 17, the time-averaged streamwise velocities in these two cases both reach the minimum value at around $X/L = 0.2$. It means that the magnitude of streamwise velocity deficit is the largest at this position. In the flexible plate case, there is a recirculation zone before around $X/L = 0.9$. But in the rigid plate case, the recirculation zone exists until around $X/L = 1.9$. In Fig. 18, the streamwise velocity deficits in these two cases both decrease gradually at these four positions. Besides, the magnitude and vertical ranges of velocity deficit in the flexible plate case are less than those in the rigid case at each streamwise position. Specifically, both rigid and flexible plate cases suffer a great velocity deficit at $X/L = 0.4$. The negative streamwise velocity at around $Y/L = 0$ indicates that there is a recirculation zone. At $X/L = 1.8$, the streamwise velocity in the flexible case restores to be positive, but the minimum streamwise velocity in the rigid case is still negative. It is also found that the time-averaged streamwise velocity distributions at lower Re_D are similar. Therefore, the flexible trailing-edge plate could greatly reduce the velocity deficit in the wake region, thus may lead to drag reduction compared with the rigid trailing-edge plate.

The Re_D effects are further considered in Fig. 19, where the time-averaged streamwise velocity distributions at the
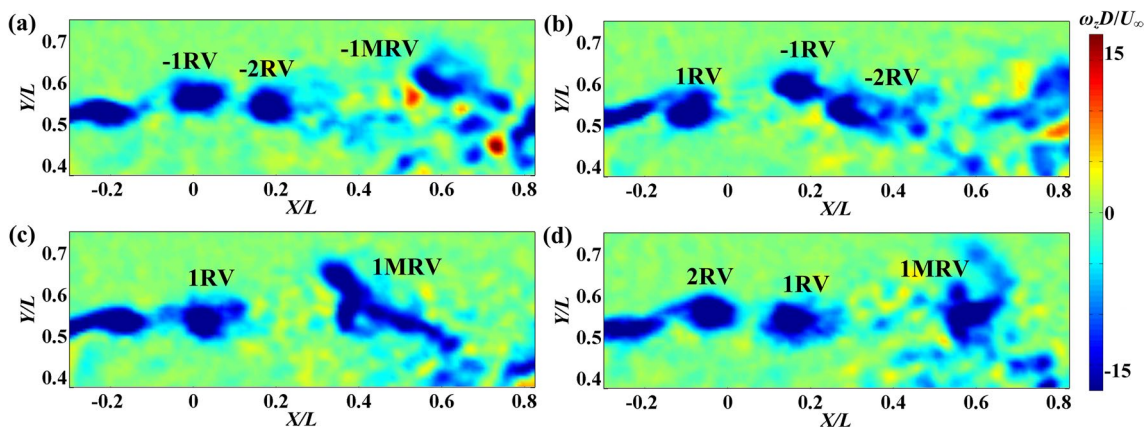
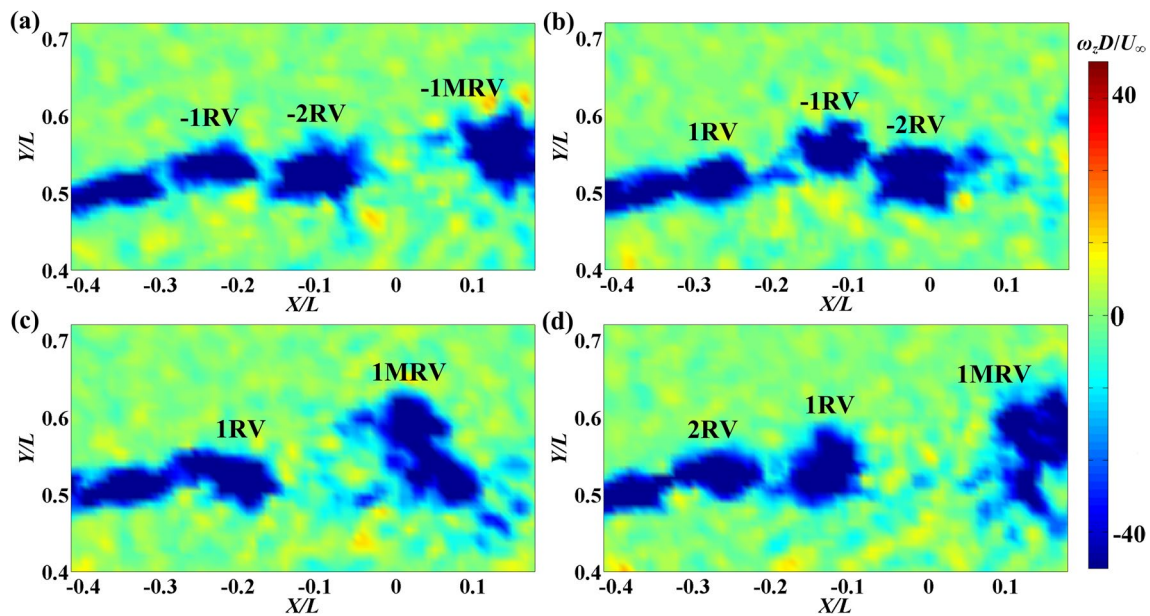**Fig. 15** Instantaneous vorticity contour of local flow field at $Re_D = 1.42 \times 10^4$

Fig. 16 Instantaneous vorticity contour of local flow field at $Re_D = 2.84 \times 10^4$
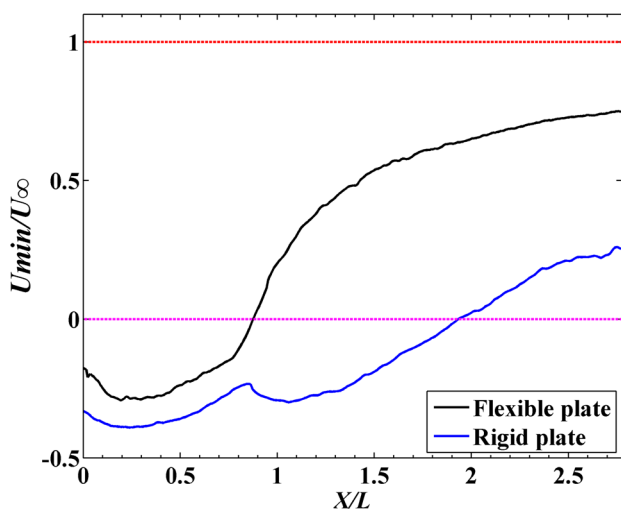

Fig. 17 The minimum value evolution of time-averaged streamwise velocity as flow goes downstream at $Re_D = 3.57 \times 10^4$

certain position $X/L = 1.1$ are presented with different marks. U_∞ at different Re_D cases are used for nondimensionalization. It can be seen that the velocity deficit is the largest when $Re_D = 1.42 \times 10^4$. With the increase of Re_D, the velocity deficit decreases. It is found that this phenomenon also exists at other positions in the wake region, which implies the velocity deficit becomes smaller at higher Re_D.

The root mean square distributions of streamwise (u_{rms}) and vertical (v_{rms}) velocity fluctuations at $X/L = 1.1$ are shown in Fig. 20a and b. The black and blue lines represent the flexible and rigid plate cases, respectively. u_{rms} and v_{rms}

are nondimensionalized by U_∞. In Fig. 20a, u_{rms} presents a double-peak distribution in both flexible and rigid plate cases. Specifically, the first peak appears near $Y/L = 0.4$, where the difference is little between the flexible and rigid cases. Considering the vortex structures shown in Fig. 9, $Y/L = 0.4$ is close to the vertical position where the leading-edge vortex sheds in the wake region. The second peak appears near $Y/L = 0$ in the flexible case, corresponding to the vertical position where the trailing-edge vortex sheds. In the rigid case, the second peak is located near $Y/L = -0.6$. Due to the bending of the flexible plate in the process of the trailing-edge vortex shedding, the distance between the double peaks is smaller in the flexible case. Moreover, at the same Re_D, the peak value of u_{rms} in the flexible case is larger than that in the rigid case. For different Re_D, the vertical positions of the double peaks are basically unchanged, which indicated that Re_D has little influence on the vertical shedding positions of the leading- and trailing-edge vortices.

In Fig. 20b, the double-peak distribution of v_{rms} in the rigid case is similar to u_{rms} in Fig. 20a. However, v_{rms} performs a single-peak distribution in the flexible case, which is distinctly different from that in the rigid case. This single-peak distribution indicates the periodic fluctuation of vertical velocity caused by the alternate shedding of the leading- and trailing-edge vortices in the wake region. It can also be found that the amplitude of the single peak is obviously larger than each amplitude of the double peaks.

Furthermore, the Reynolds shear stress ($-\overline{u'v'}$) distributions at $X/L = 1.1$ are presented in Fig. 20c. The positive peak values of the Reynolds shear stress in both two cases appear near $Y/L = 0.4$. The negative peak value in the flexible

Fig. 18 Time-averaged stream-
wise velocity distributions at
$Re_D = 3.57 \times 10^4$. **a** $X/L = 0.4$;
b $X/L = 1.1$; **c** $X/L = 1.8$; **d**
$X/L = 2.5$
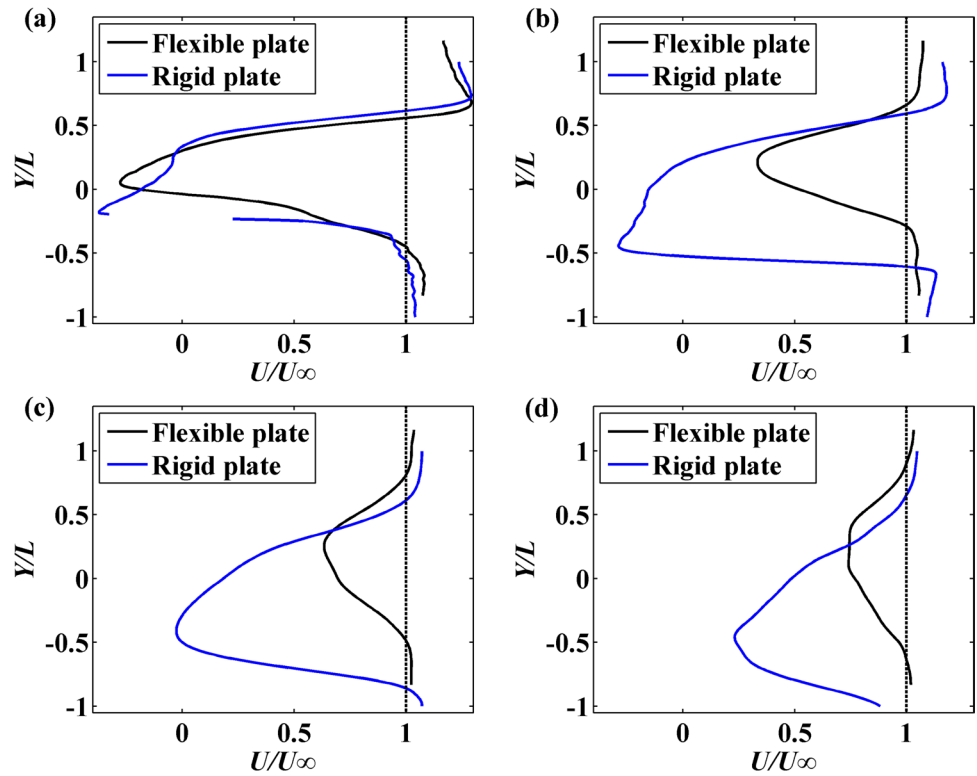
Fig. 19 Time-averaged stream-
wise velocity distributions at
$X/L = 1.1$ ($Re_D = 1.42 \times 10^4$,
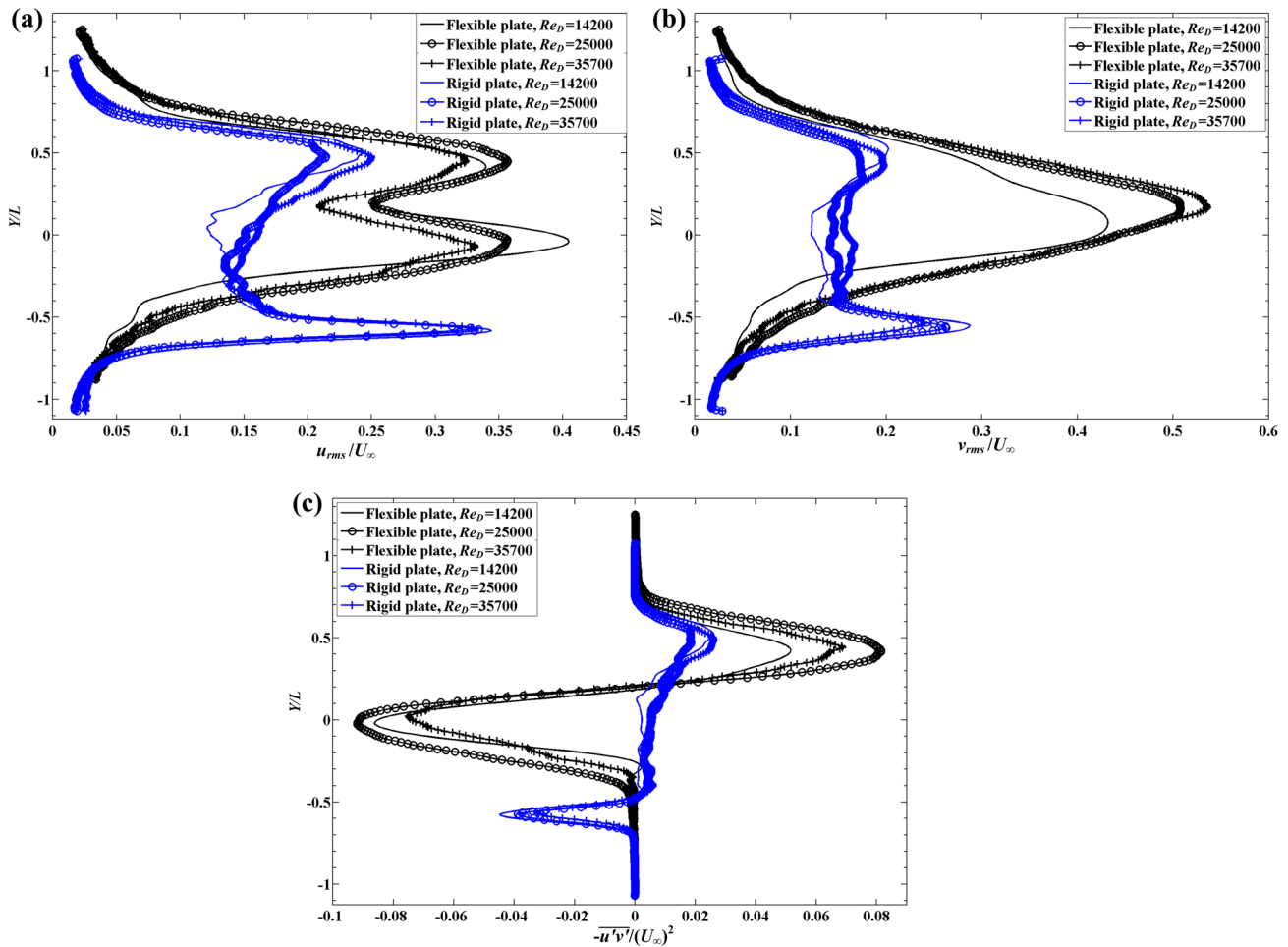2.5×10^4 and 3.57×10^4)
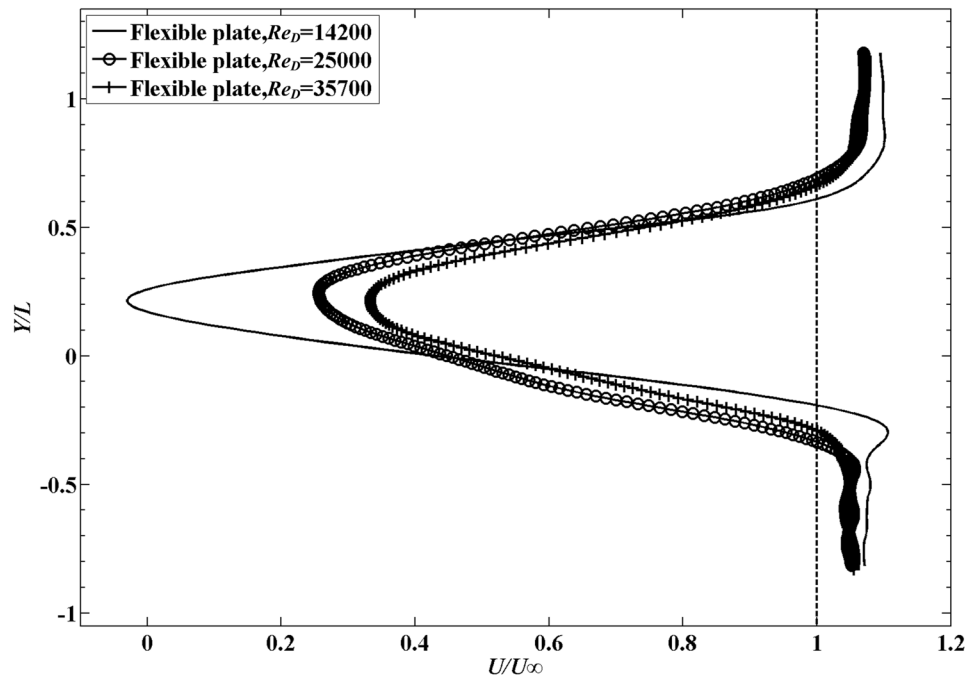
case occurs near $Y/L = 0$, while near $Y/L = -0.6$ in the rigid case. The results are in accordance with Fig. 20a. In addition, the absolute values of the peaks in the flexible plate case are much larger than those in the rigid case.

In Fig. 20, the much larger peak values in the flexible plate case indicate that the velocity fluctuations are stronger than the rigid plate case. Actually, it is because that the vibration of the flexible plate strengthens the momentum exchange of the fluid in the wake region.

Fig. 20 Statistical characteristics of fluctuations in the flexible and rigid cases at $X/L = 1.1$ ($Re_D = 1.42 \times 10^4$, 2.5×10^4 and 3.57×10^4). **a** Root mean square distributions of streamwise velocity fluctuation; **b** root mean square distributions of vertical velocity fluctuation; **c** Reynolds shear stress distributions

3.6 Fluid–structure coupling

It was mentioned in Sect. 3.3 that the generation and shedding processes of the leading- and trailing-edge vortices occurred only once in one flow cycle. Considering the phase-averaged flow field was based on the motion of the flexible plate, the shedding frequencies of the leading- (f_{LEV}) and trailing- (f_{TEV}) edge vortices were conjectured to be consistent with the vibration frequency of the plate. To support this conjecture, the frequency characteristics of the wake region were analyzed.

As mentioned in Fig. 20, the vertical positions of the double peaks of u_{rms} corresponded to the shedding positions of the leading- and trailing-edge vortices. Therefore, the streamwise velocity signals at the positions of the double peaks at $X/L = 1.1$ were used to conduct FFT analysis, which are shown in Fig. 21. It can be seen that f_{LEV} is equal to f_{TEV} at the same Re_D. With Re_D increasing, the corresponding f_{LEV} and f_{TEV} also increase, which are 0.62 Hz, 0.88 Hz and 1.54 Hz, respectively, in Fig. 21. These frequencies are in accordance with the vibration frequencies of the plate in Table 1.

Further evidence for the consistence between the frequencies of the wake region and the plate could be obtained by the global FMD method. Due to the similarity in all Re_D cases tested, $Re_D = 1.42 \times 10^4$ was selected as an example. The power spectrum of the global flow field at $Re_D = 1.42 \times 10^4$ is shown with blue curve in Fig. 22. Meanwhile, the power spectrum of the flexible plate is taken as a contrast in red curve. It can be found that the dominant frequency of the global flow field ($f = 0.62$ Hz) is consistent with the flexible plate, which indicates the flow field and the flexible plate vibration have reached a coupling state. Besides, there are two small peaks at $f = 1.21$ Hz and $f = 1.83$ Hz in the global power spectrum. The two peaks are exactly the second and third harmonics of the dominant frequency. When $f > 1.83$ Hz, there are not any obvious peaks in the spectrum.
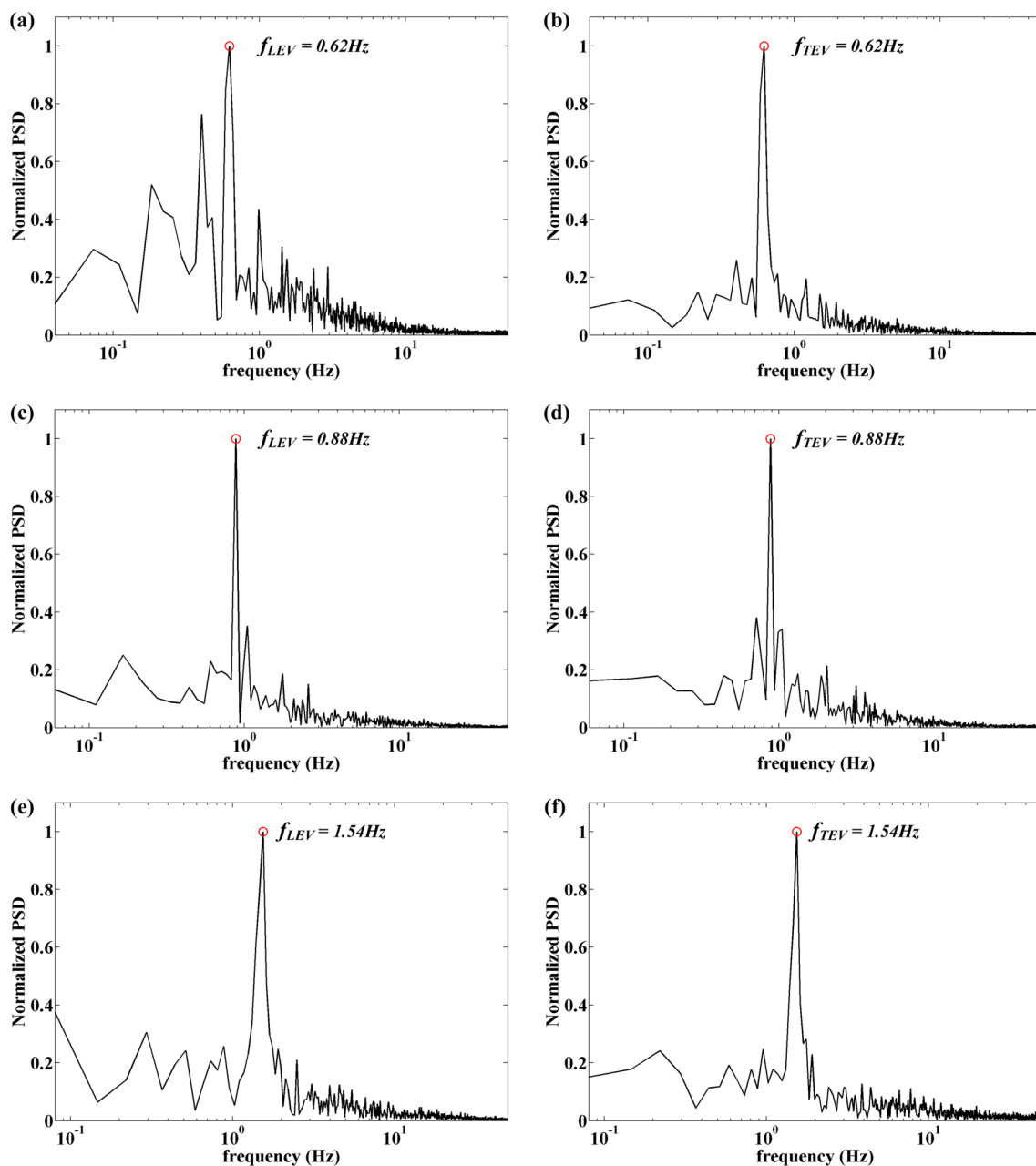
Fig. 21 Frequency spectra of the leading- and trailing-edge vortices. **a, b** $Re_D = 1.42 \times 10^4$; **c, d** $Re_D = 2.5 \times 10^4$; **e, f** $Re_D = 3.57 \times 10^4$; **a, c, e** leading-edge vortex; **b, d, f** trailing-edge vortex

Then the Fourier mode based on vertical velocity at the dominant frequency ($f = 0.62$ Hz) is illustrated in Fig. 23. It can be seen that the mode is very large and symmetric about streamwise direction. Besides, this Fourier mode is concentrated in the wake region. According to Ma et al. (2015), the Fourier mode based on the characteristic frequency actually reflects the fluctuation characteristics of the periodic mean component and the contributions of large-scale organized coherent structures. The symmetry characteristic

with respect to the vertical velocity component in Fig. 23 is related to asymmetric shedding process of the leading- and trailing-edge vortices.

Referring to Timpe et al. (2013) and Bleischwitz et al. (2017), cross-correlation between the flexible plate and the velocity field was conducted to study fluid–structure coupling. The vertical displacement at the end of the flexible plate was selected as the correlation signal. Therefore, Eq. (5) can be rewritten as
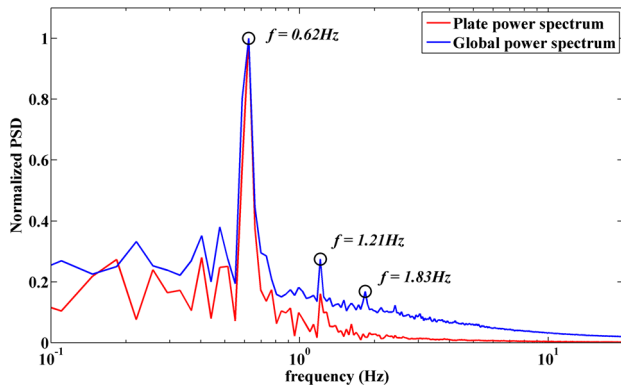
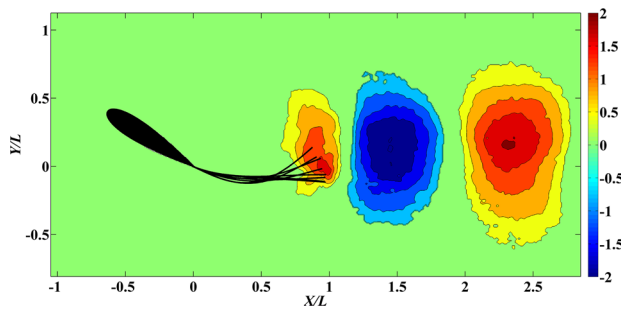**Fig. 22** Power spectrum of the global flow field at $Re_D = 1.42 \times 10^4$

Fig. 23 Global Fourier mode based on vertical velocity at $Re_D = 1.42 \times 10^4$

$$R_{y'v'}(x_0, y_0, x_1, y_1, t) = \frac{\overline{y'(x_0, y_0, t) v'(x_1, y_1, t)}}{\sigma_{y'}\sigma_{v'}}, \tag{8}$$

where y' is the vertical plate displacement fluctuations at the plate end, v' is the vertical velocity fluctuations at every mesh node. It should be noticed that Eq. (8) is reduced to spatial cross-correlation with zero time lag due to $\tau = 0$. As a result, the positive and negative correlation coefficients can, respectively, indicate the in-phase and out-of-phase relationships between the plate vibration and the velocity field.

As shown in Fig. 24, y' and the global v' were calculated as cross-correlation coefficient contours for $Re_D = 1.42 \times 10^4$, 2.5×10^4 and 3.57×10^4. In each figure of Fig. 24, there exists a large positive, highly correlated region near the plate end at around $X/L = 1$, which means an upwards plate movement comes with an instantaneous vertically upwards directed flow and vice versa. The large negative and positive alternating correlated region in the wake at $X/L > 1.2$ represents the asymmetric wake vortex-shedding process. Moreover, there is a large negative correlated region in the recirculation zone at the leeward airfoil surface in all of these Re_D cases. The size of negative correlated region at the leeward airfoil surface is larger at higher Re_D cases. This means the influence of the plate vibration is enhanced and propagates to a more advanced location at higher Re_D cases.

Overall, it can be concluded by frequency and cross-correlation analyses that the vortex-shedding processes
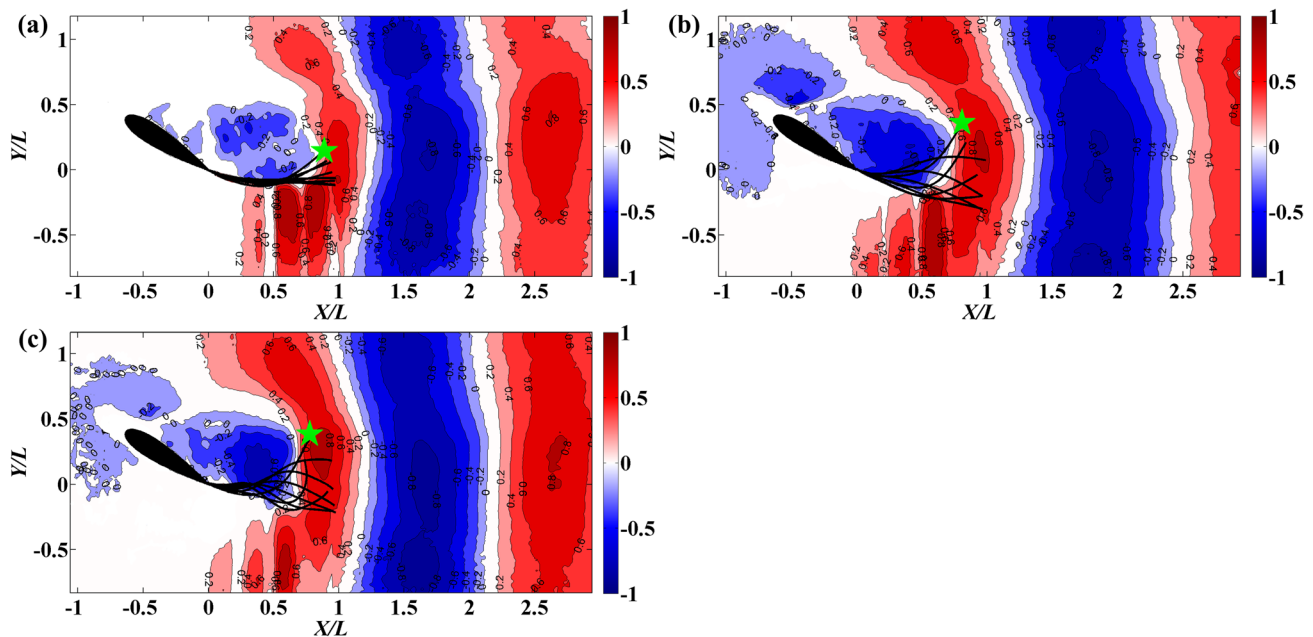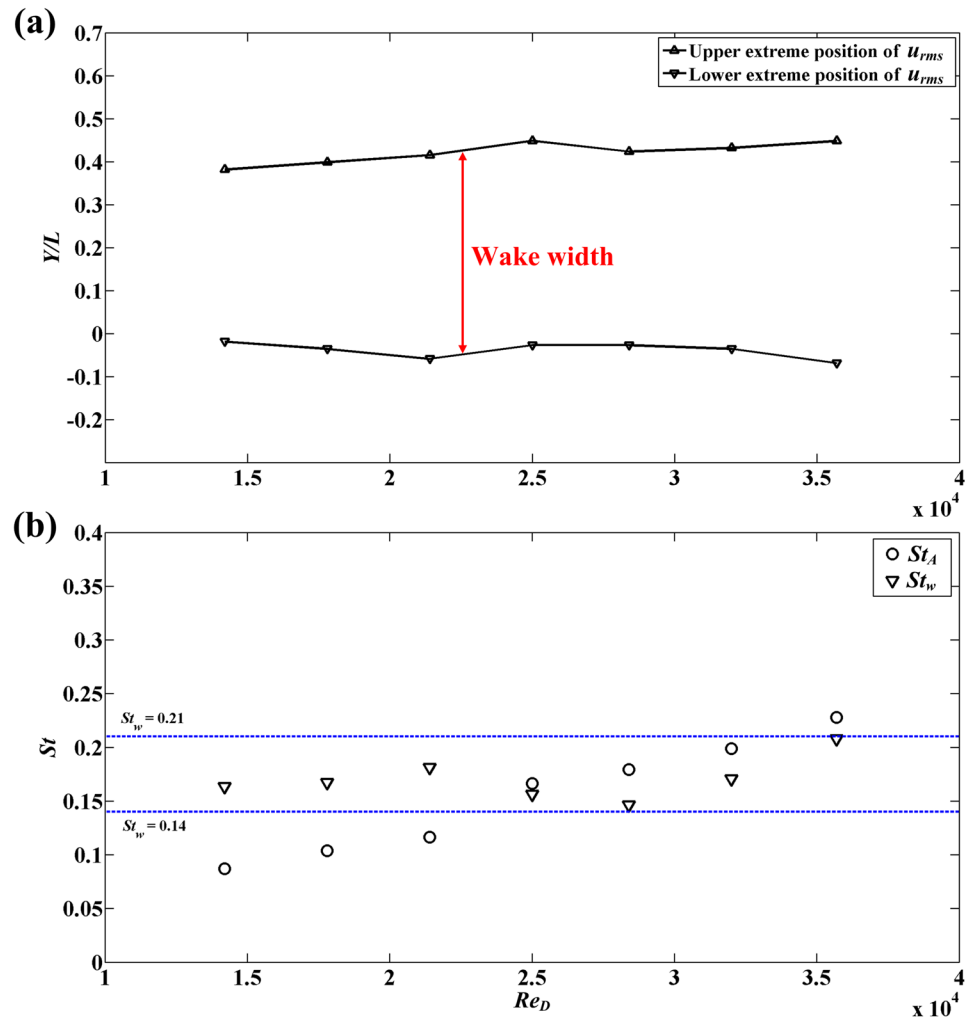

Fig. 24 Cross-correlation between vertical plate fluctuations at the plate end and global vertical velocity fluctuations. The plate end is indicated with the green pentagram. **a** $Re_D = 1.42 \times 10^4$; **b** $Re_D = 2.5 \times 10^4$; **c** $Re_D = 3.57 \times 10^4$

Fig. 25 Variations of wake width and the corresponding Strouhal number

4 Discussion

As mentioned above, the vibration pattern of the plate seemed to present more complicated deformation and larger amplitude with the increase of Re_D. The vibration frequencies of the flexible plate also varied with Re_D. However, the evolution processes of the leading- and

are coupled with the vibration of the plate in the wake region. The mechanism of this fluid–structure coupling is found to be basically the same in all Re_D cases tested in this study. Actually, the vibration of the flexible plate has a dominant effect on the wake region, causing the asymmetric shedding process of the leading- and trailing-edge vortices. This asymmetric vortex-shedding mode is similar to the Von Kármán vortex-shedding around the bluff body. Consequently, the fluid–structure coupling leads the flow field to form a bluff-body wake.

trailing-edge vortices, the wake vortex-shedding mode and the mechanism of fluid–structure coupling were basically the same in all Re_D cases tested in this study. Therefore, a conflict between the deformation and the flow field appears.

In Sect. 3.1, this paper has tried to scale the vibration frequencies of the flexible plate and find similarities among the frequencies at various Re_D. Strouhal number based on vibration amplitude (St_A) was calculated as a comprehensive nondimensional parameter. However, St_A showed a highly linear correlation with Re_D, which failed to scale the vibration frequencies.

So another Strouhal number based on the wake width (St_w) was proposed in this section. Referring to Roshko (1954) and Griffin (1978), the wake width could be defined as the vertical distance between the maxima of the velocity fluctuations at the end of vortex formation. As a result, St_w could be calculated. St_w was further introduced by Roshko (1954) and Yarusevych et al. (2009) to be a "universal" Strouhal number for scaling the vortex-shedding

frequencies. Here, the upper and lower maximum positions of u_{rms} at $X/L = 1.1$ and the variation of St_w are shown in Fig. 25. It can be seen in Fig. 25a that the wake width basically keeps constant at various Re_D. In Fig. 25b, St_w presents relatively constant values, which are in the range of 0.14–0.21. This Strouhal range is precisely the range for various bluff bodies and Reynolds numbers (Roshko 1954; Morse and Liburdy 2009). This agreement exactly indicates that all cases tested in this paper present a vortex-shedding process similar to typical bluff-body wakes. This is probably due to the high angle of attack ($\alpha = 30°$), which corresponds to completely separated flow for all cases tested (Abernathy 1962). This finding further confirms that the nature of fluid–structure coupling leads the flow field to form a bluff-body wake. The influence of the flexible trailing-edge plate is enhanced with Re_D increasing, causing more complicated deformation, but the essential mechanism remains unchanged.

5 Conclusion

This paper discussed the effect of flexible trailing-edge plate on the flow structures of an airfoil and the corresponding fluid–structure coupling phenomenon at high angle of attack ($\alpha = 30°$). The vibration of the flexible plate was explored to be a great disturbance to the flow field, which not only had a dominant influence on the wake region, but also could propagate towards upstream. This disturbance significantly influenced the flow structures of the airfoil.

1. The kinematic characteristics of the flexible plate were firstly analyzed. It was found that the vibration of this flexible plate was a strongly periodic motion. The vibration pattern of the plate presented more complicated deformation and larger amplitude with the increase of Re_D. The vibration frequencies of the flexible plate also increased with Re_D. With the aim of scaling the vibration frequencies, Strouhal number based on vibration amplitude (St_A) was calculated as a comprehensive nondimensional parameter. However, St_A showed a highly linear correlation with Re_D, which failed to scale the vibration frequencies of the flexible plate at various Re_D.

2. From the measured flow field, the evolution processes of flow structures including the leading- and trailing-edge vortices around the airfoil were investigated. On the one hand, the trailing-edge vortex generated and accumulated beneath the flexible plate and then shed from the plate and dissipated downstream. On the other hand, the leading-edge vortex was generated from the coherent structures in the separated shear layer. Subsequently, the shear layer was hindered by the trailing-edge

vortex and gradually evolved into a leading-edge vortex. Besides, it was found that the airfoil attached with a flexible trailing-edge plate could reduce the velocity deficit in the wake region and suppress the post-stall separation compared with the rigid plate.

3. The vortex-shedding processes were coupled with the vibration of the plate in the wake region. Actually, the vibration of the flexible plate had a dominant effect on the wake region, causing the asymmetric shedding process of the leading- and trailing-edge vortices. This asymmetric vortex-shedding mode is similar to the Von Kármán vortex-shedding around the bluff body. Consequently, the fluid–structure coupling led the flow field to form a bluff-body wake.

4. The evolution processes of the leading- and trailing-edge vortices, the wake vortex-shedding mode and the mechanism of fluid–structure coupling were analyzed to be basically the same in all Re_D cases tested in this study. Considering the failure of St_A on scaling the vibration frequencies, another Strouhal number based on the wake width (St_w) was proposed in this paper. As found, St_w presented relatively constant values, which were in the range of 0.14–0.21. This Strouhal range was precisely the range for various bluff bodies and Reynolds numbers. This agreement exactly indicated that all cases tested in this paper presented a bluff-body wake, which was consistent with the vortex-shedding mode and the fluid–structure coupling.

References

Abernathy FH (1962) Flow over an inclined plate. ASME J Basic Eng 84:380–388

Adrian RJ, Christensen KT, Liu ZC (2000) Analysis and interpretation of instantaneous turbulent velocity fields. Exp Fluids 29(3):275–290

Allen JJ, Smits AJ (2001) Energy harvesting eel. J Fluid Struct 15:629–640

Anderson JM, Streitlien K, Barrett DS, Triantafyllou MS (1998) Oscillating foils of high propulsive efficiency. J Fluid Mech 360:41–72

Blake R (1983) Fish locomotion. Cambridge Univ. Press, Cambridge

Bleischwitz R, De Kat R, Ganapathisubramani B (2017) On the fluid-structure interaction of flexible membrane wings for MAVs in and out of ground-effect. J Fluid Struct 70:214–234

Cantwell B, Coels D (1983) An experimental study of entrainment and transport in the turbulent near wake of a circular cylinder. J Fluid Mech 136:321–374

Champagnat F, Plyer A, Le BG, Leclaire B, Davoust S, Le Saut Y (2011) Fast and accurate PIV computation using highly parallel iterative correlation maximization. Exp Fluids 50(4):1169–1182

Connell B, Yue D (2007) Flapping dynamics of a flag in a uniform stream. J Fluid Mech 581:33–68

David MJ, Govardhan RN, Arakeri JH (2017) Thrust generation from pitching foils with flexible trailing edge flaps. J Fluid Mech 828:70–103

Deng SC, Pan C, Wang JJ, Rinoshika A (2017) POD analysis of the instability mode of a low-speed streak in a laminar boundary layer. Acta Mech Sin 33(6):981–991

Dewey PA, Boschitsch BM, Moored KW, Stone HA, Smits AJ (2013) Scaling laws for the thrust production of flexible pitching panels. J Fluid Mech 732:29–46

Eloy C, Souilliez C, Schouveiler L (2007) Flutter of a rectangular plate. J Fluid Struct 23:904–919

Eloy C, Lagrange R, Souilliez C, Schouveiler L (2008) Aeroelastic instability of cantilevered flexible plates in uniform flow. J Fluid Mech 611:97–106

Giacomell A, Porfiri M (2011) Underwater energy harvesting from a heavy flag hosting ionic polymer metal composites. J Appl Phys 109(8):084903

Griffin OM (1978) An universal Strouhal number for the "locking-on" of vortex shedding to the vibrations of bluff cylinders. J Fluid Mech 85(3):591–606

Heathcote S, Gursul I (2007) Flexible flapping airfoil propulsion at low Reynolds numbers. AIAA J 45(5):1066–1079

Katz J, Weihs D (1978) Hydrodynamic propulsion by large amplitude oscillation of an airfoil with chordwise flexibility. J Fluid Mech 88(3):485–497

Kim W, Yoo JY, Sung J (2006) Dynamics of vortex lock-on in a perturbed cylinder wake. Phys Fluids 18(7):1–22

Lighthill MJ (1970) Aquatic animal propulsion of high hydromechanical efficiency. J Fluid Mech 44(2):265–301

Lindsey CC (1978) Form, function and locomotory habits in fish. Fish Physiol 7:1–100

Liu TS, Montefort J, Liou W, Pantula SR, Shams QA (2007) Lift enhancement by static extended trailing edge. J Aircraft 44(6):1939–1947

Liu TS, Montefort J, Liou W, Pantula SR, Yang Y and Shams QA (2009) Post-stall flow control using a flexible fin on airfoil. In: 47th Asia Aerospace Sciences Meeting. 5–8 Jan 2009, Orlando, Florida

Liu TS, Montefort J, Pantula SR (2010) Effects of flexible fin on low-frequency oscillation in poststall Flows. AIAA J 48(6):1235–1247

Ma LQ, Feng LH, Pan C, Gao Q, Wang JJ (2015) Fourier mode decomposition of PIV data. Sci China Technol Sc 58:1935–1948

Mackowski AW, Williamson CHK (2015) Direct measurement of thrust and efficiency of an airfoil undergoing pure pitching. J Fluid Mech 765:524–543

Miyanawala TP, Jaiman RK (2019) Decomposition of wake dynamics in fluid-structure interaction via low-dimensional models. J Fluid Mech 867:723–764

Morse DR, Liburdy JA (2009) Vortex dynamics and shedding of a low aspect ratio, flat wing at low Reynolds numbers and high angles of attack. J Fluid Eng T ASME 131(5):051202

Pan C, Xue D, Xu Y, Wang JJ, Wei RJ (2015) Evaluating the accuracy performance of Lucas–Kanade algorithm in the circumstance of PIV application. Sci China Phys Mech 58(10):1–16

Pantula SR (2008) Modeling fluid structure interaction over a flexible fin attached to a NACA0012 airfoil. Ph.D. Thesis, Department of Mechanical and Aeronautical Engineering, Western Michigan University, Kalamazoo, MI, 2008

Roshko A (1954) On the drag and shedding frequency of two dimensional bluff bodies. NACA Technical Note 3169

Sfakiotakis M, Lane DM, Davies JBC (1999) Review of fish swimming modes for aquatic locomotion. IEEE J Ocean Eng 24(2):237–252

Shelley MJ, Zhang J (2011) Flapping and bending bodies interacting with fluid flows. Annu Rev Fluid Mech 43(1):449–465

Shelley MJ, Vandenberghe N, Zhang J (2005) Heavy flags undergo spontaneous oscillations in flowing water. Phys Rev Lett 94(9):094302

Timpe A, Zhang Z, Hubner J, Ukeliey L (2013) Passive flow control by membrane wings for aerodynamic benefit. Exp Fluids 54(3):1471

Triantafyllou MS, Triantafyllou GS, Gopalkrishnan R (1991) Wake mechanics for thrust generation in oscillating foils. Phys Fluids 3(12):2835–2837

Triantafyllou MS, Triantafyllou GS, Yue DKP (2000) Hydrodynamics of fishlike swimming. Annu Rev Fluid Mech 32(1):33–53

Triantafyllou MS, Techet AH, Hover FS (2004) Review of experimental work in biomimetic foils. IEEE J Oceanic Eng 29(3):585–594

Wang JS, Feng LH, Wang JJ, Li T (2018) Görtler vortices in low-Reynolds-number flow over multi-element airfoil. J Fluid Mech 835:898–935

Watanabe Y, Suzuki S, Sugihara M, Sueoka Y (2002) An experimental study of paper flutter. J Fluid Struct 16:529–542

Wolfgang M, Anderson JM, Grosenbaugh MA, Yue DKP, Triantafyllou MS (1999) Nearbody flow dynamics in swimming fish. J Exp Biol 202(17):2303–2327

Wu T (1971) Hydromechanics of swimming propulsion. Part 1. Swimming of a two-dimensional flexible plate at variable forward speeds in an inviscid fluid. J Fluid Mech 46(2):337–355

Yarusevych S, Sullivan PE, Kawall JG (2006) Coherent structures in an airfoil boundary layer and wake at low Reynolds numbers. Phys Fluids 18:044101

Yarusevych S, Sullivan PE, Kawall JG (2009) On vortex shedding from an airfoil in low-Reynolds-number flows. J Fluid Mech 632:245–271

Zhang J, Childress S, Libchaber A, Shelley M (2000) Flexible filament in a flowing soap film as a model for one-dimensional flags in a two-dimensional wind. Nature 408:835–839

Zhou Y, Yiu MW (2006) Flow structure, momentum and heat transport in a two-tandem-cylinder wake. J Fluid Mech 548:17–48

Zhou J, Adrian RJ, Balachandar S, Kendall TM (1999) Mechanisms for generating coherent packets of hairpin vortices in channel flow. J Fluid Mech 387:353–396

Zhou Y, Zhang HJ, Yiu MW (2002) The turbulent wake of two side-by-side circular cylinders. J Fluid Mech 458:303–332